5 The Radiobiology of Radiopharmaceutical Therapy: The Input of Imaging and Radiomics

Jean-Pierre Pouget, Marion Tardieu, and Sophie Poty

5.1 Introduction

Radiopharmaceutical therapy (RPT) is a modality in which radiolabelled cancer-targeted biomolecules are used to specifically irradiate tumour cells [1]. The approach is particularly useful for the treatment of metastatic or diffuse tumours, i.e. situations in which conventional external beam radiotherapy (EBRT) would expose normal tissues to intolerable doses. Depending on the decay spectrum of the radionuclide, RPT can be categorized as alpha (α), beta (β) or Auger electron (AE) RPT. However, most radionuclides emit a mixture of radiation types that also includes gamma (γ) rays, X-rays or internal conversion electrons (ICE). Unlike EBRT, which uses low linear energy transfer (LET) radiation, RPT offers the possibility of using both low- and high-LET particles with ranges generally below 1.5 cm [2]. In theory, RPT is most suitable for the treatment of small volume tumours because of 'volume effects', i.e. for a same physical absorbed dose, RPT is expected to be more efficient at treating smaller tumours than larger ones. Another distinct feature of RPT irradiation is a heterogeneous dose distribution in time and space that is dependent on (i) the pharmacokinetic profile of the radiopharmaceutical, (ii) the physical half-life of the radionuclide and (iii) the range of emitted particles. Importantly, RPT generally delivers continuous low dose rate (CLDR) irradiation (< 1 Gy/h), which can be compared to some extent to low dose rate brachytherapy.

Taken together, the distinct features of RPT merit the reconsideration of current radiobiology paradigms that are predominantly based on data from EBRT [3, 4]. After a century of work, the latter is predicated largely on the 'target cell' theory as well as DNA as the primary mediator of radiation-induced cytotoxicity (Fig. 5.1). Yet, it is now clear that subcellular compartments other than the nucleus should be considered to be mediators of cytotoxicity and that cell death mechanisms that originate both close to (i.e. bystander effects) and farther from (i.e. the immune response) irradiated cells are at work as well (Fig. 5.1). As a result, it becomes clear that a more integrated view of radiation biology is needed and that the contribution of non-targeted radiation effects needs to be assessed in patients. While radiobiology is mostly evaluated in vitro or ex vivo, there is a critical need to develop non-invasive approaches that allow for the real-time in vivo monitoring of radiation-induced biological events during RPT. In recent years, molecular imaging has played a critical role in the measurement of molecular and cellular processes in humans and other living systems.

J.-P. Pouget (✉) · M. Tardieu · S. Poty (✉)
Institut de Recherche en Cancérologie de Montpellier (IRCM), INSERM U1194, Université de Montpellier, Institut Régional du Cancer de Montpellier (ICM), Montpellier, France
e-mail: jean-pierre.pouget@inserm.fr; marion.tardieu@inserm.fr; sophie.poty@inserm.fr

L. Bodei et al. (eds.), *Radiopharmaceutical Therapy*, https://doi.org/10.1007/978-3-031-39005-0_5

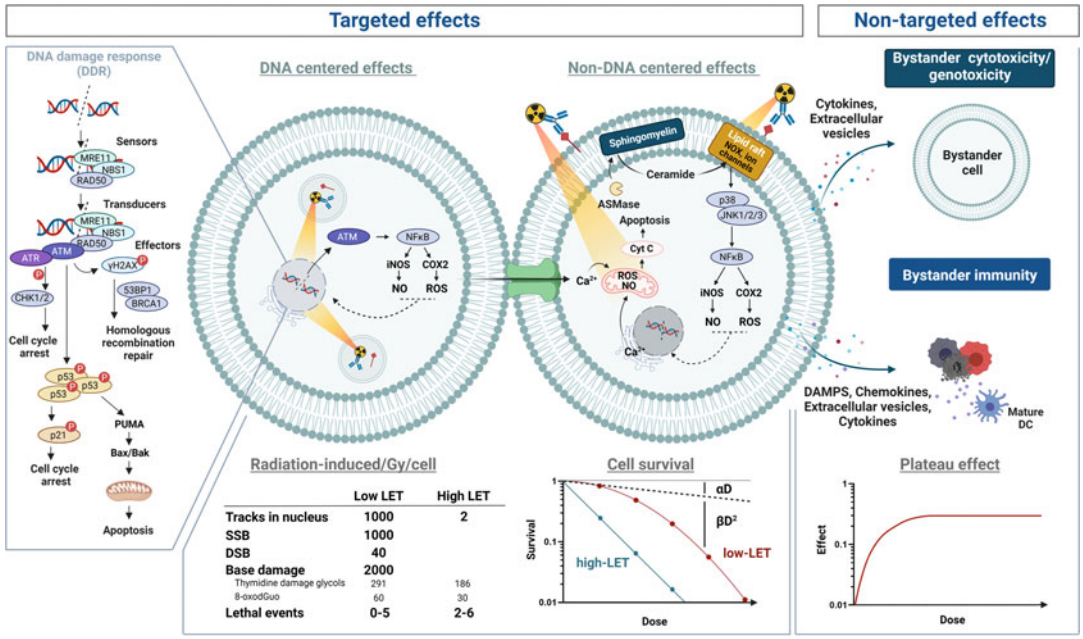

Fig. 5.1 General overview of the targeted and non-targeted effects induced by RPT. (Adapted from [3]). Created with BioRender.com

Indeed, imaging allows for the non-invasive monitoring of anatomical and functional parameters and may offer new resources to improve RPT. From medical images, radiomics extracts a high number of quantitative features and explores potential associations with biology and clinical outcomes when coupled to mathematical methods and artificial intelligence (AI) algorithms. In these pages, we will work to identify established and potential molecular imaging probes that may help delineate radiobiological events and thus augment our understanding of the radiobiology of RPT.

5.2 The Fundamentals of Radiobiology

With a few notable exceptions (e.g. radioactive iodide, radium), RPT requires the development of radiopharmaceuticals based on tumour-targeting vectors – e.g. monoclonal antibodies, peptides, small molecules – that are labelled with radionuclides. Since the 1950s, the choice of radionuclide was generally dictated by practical considerations, such as availability and ease of handling. Furthermore, very little concern was devoted to the administration schedule of RPT and its dosimetry. Until recently, in preclinical models but also in the clinic, one single injection was generally performed; the mean absorbed doses to normal tissues or tumours were not systemically calculated; and considerations related to the total absorbed dose, dose fractionation, overall treatment time and volume effects were not considered. Simply put, the concepts of radiobiology have historically been ignored.

5.2.1 Overview of EBRT Clinical Radiobiology: An Empirical Experience

While RPT is fundamentally different from EBRT, the former has certainly benefitted from the latter's century of experience. A tremendous number of patients have been treated with a large number of EBRT schemes, allowing for the optimization of various radiotherapy parameters. In

contrast, although increasing, the number of patients treated with RPT remains relatively low.

To better understand what could or should be done in the context of RPT, it is interesting to note that the beginnings of EBRT have been empirical and somewhat random. The first cancer patients were treated with EBRT as early as 1896 by Victor Despeignes in Lyon [5]. Because of the very low output of X-ray tubes, most of the dose was delivered to the skin, then the dose-limiting organ. Skin was shown to have two types of response: (i) erythema and moist desquamation occurring several days/weeks after irradiation (early effects) and (ii) telangiectasia occurring several months after exposure (late effects). As dose rates were not yet calculated, erythema, moist desquamation and telangiectasia were used as the biological endpoints of normal tissue tolerance. Progressively, preclinical studies have been conducted to better understand the effects of radiation at the cellular level.

One of the first principles of radiobiology comes from the studies of Regaud, who irradiated human testis and observed that spermatogonia rather than spermatozoids exhibited the greatest effects [5]. These data were followed by Bergonie and Tribondeau's law that 'the radiosensitivity of a biological tissue is directly proportional to the mitotic activity and inversely proportional to the degree of differentiation of its cells' [5]. The principle of dose fractionation was introduced in 1928 by Krönig and Friedrich, who showed that the dose required to observe a skin reaction is higher when it is fractionated, suggesting that the skin can recover when the dose is delivered over several days [5]. Several years later, Coutard showed that, at specific doses, the reaction of the skin and mucosa depended on the total treatment duration, and the latter parameter became another principle of radiotherapy [5]. Furthermore, Baclesse observed that if the dose is limited to certain levels, skin mucositis and moist desquamation does not take place at 2.5 weeks and 6 weeks [5]. As a result, a second cycle can be given after 6 weeks, and higher doses can be given over a longer period. Treatments were then progressively optimised by varying the dose, the dose fraction and the intervals between fractions so that the treatment duration was longer. Finally, Coutard arrived at dose-time-fractionation schedules close to those that are now regarded as a standard fractionation schedule: 2 Gy per fraction with daily fractionation over 6–7 weeks [5].

In the 1980s, the question of tissue radiosensitivity was first raised. The response of early- and late-responding normal tissues to each fraction was shown to differ. Therefore, dose hyperfractionation – e.g. the administration of 1.15 Gy per fraction three times per day with 4–6 h between fractions over 7–8 weeks – was adopted to exploit the differences in sensitivity between early-responding tissues (e.g. tumour, skin [erythema], bone marrow or kidney) and late-responding tissues (e.g. skin [telangiectasia], lung, jejunum, colon). This difference is due to the greater ability of some cells to repair damage at the molecular level between fractions.

5.2.2 The Linear Quadratic (LQ) Model of EBRT: Can We Extrapolate to RPT?

As EBRT aims at eradicating clonogenic tumour cells, the clonogenic assay developed by Puck and Marckus in the 1950s was immediately considered the reference technique for measuring the ability of irradiated cells to form colonies (i.e. determining clonogenic survival) [6]. In mammalian cells exposed to low-LET radiation, the curve of clonogenic survival vs. dose is a biphasic exponential (Fig. 5.1). In a semi-logarithmic plot, this survival curve is composed of a linear slope (i.e. the α parameter) followed by a curvature or shoulder at increasing doses (i.e. the β parameter). The parameter α (expressed in Gy^{-1}) corresponds to the intrinsic radiosensitivity of the cell (i.e. the probability per Gy for a cell to be killed when its sensitive target is crossed by a particle). The parameter β (expressed in Gy^{-2}) is related to the ability of the cell to repair radiation-induced damage (i.e. β decreases and survival increases when cells have time to repair, for example, between fractions). In contrast, as complex lesions of high-LET

particles are not repaired, survival curves are only fitted by the α parameter. The α/β ratio is a powerful tool to predict the radiosensitivity of tissues. To wit, both tumours and early-responding tissues generally have low α/β ratios since they cannot repair damage efficiently. Late-responding tissues, in contrast, have higher α/β ratios since they can repair their lesions between fractions if given enough time.

However, it is not clear whether the clonogenic survival of cells exposed to therapeutic radiopharmaceuticals (i.e. for RPT) can be evaluated using this LQ model. To answer this question, we first need to investigate the relationships between cell absorbed dose and clonogenic survival in the context of RPT and see if α and β parameters can be determined. Parameters other than the cell absorbed dose might have to be considered, including the radiopharmaceutical intracellular distribution and the involvement of intercellular communications.

5.2.3 Low Dose Rates Require Higher Absorbed Doses: What Happens During RPT

A low dose rate is often considered the ultimate form of fractionation. Its benefit was highlighted by Coutard in 1919, when he compared the skin reactions in patients with head and neck cancer to which he delivered either one or two low dose rate fractions of X-rays per day for 2 weeks or longer [5]. Shortly thereafter, in 1922, Regaud reported the benefits of low dose rate brachytherapy of cervical cancer using radium [5]. Regaud concluded that 'alternating rhythm of cellular reproduction provides an explanation of the efficacy of prolonged irradiation'.

EBRT is usually delivered at a dose rate between 1 and 5 Gy/min such that a conventional 2 Gy dose only requires few minutes, an amount of time insufficient for cells to repair their damage. Decreasing the dose rate (0.2 Gy/min vs. 1 Gy/min) facilitates the sparing of late-responding healthy tissues (e.g. lung) [7]. Similar sparing is observed when fractionated EBRT is used at 2 Gy/fraction and even more at 1 Gy/fraction. With decreasing dose rate (< 1 Gy/min), the time required to deliver a given dose increases, and biological process can take place during irradiation and/or between fractions. For example, DNA damage repair, redistribution in the cell cycle, reoxygenation and repopulation progressively take place in the hours and days following irradiation. With low dose rates (e.g. 0.2 Gy/min dose rate, 2 Gy/fraction, 10 min treatment time), the induction of damage and repair occurs at the same time [8]. For many tumours and normal tissues, the repair half-times of sublethal damage are between 0.5 and 2 h, and complete repair generally occurs in less than 24 h (i.e. between 2 fractions of EBRT) [9]. However, some late-responding tissues may have longer repair half-times. At the cellular level, the repair half-time for base damage and DNA single-strand breaks (SSBs) is ~10 min, while that for DNA double-strand breaks (DSBs) is ~20 min. Therefore, irradiations lasting more than 10 min will significantly interfere with DNA repair. Assuming a minimal dose of 2 Gy, this corresponds to dose rates below the 0.2 Gy/min delivered by RPT. Ultimately, this creates the need, at least theoretically, for higher doses to counterbalance repair processes. Repopulation is a much slower process and depends on the doubling time of cells, which typically lies between days and weeks. Long treatment times favour the repopulation of cells from early-responding tissues such as tumours. The process will also be prominent at very low dose rates.

5.3 The Details

5.3.1 Physical Events Associated with α-/β-Particles and Auger Electrons

5.3.1.1 The Biological Effects of α-Particles Outweigh Those of Electrons and Gamma-/X-rays

In EBRT, a well-calibrated absorbed dose and dose rate of X-rays is delivered to target tissue in a collimated field. This scenario stands in stark contrast to RPT, as the decay spectra of

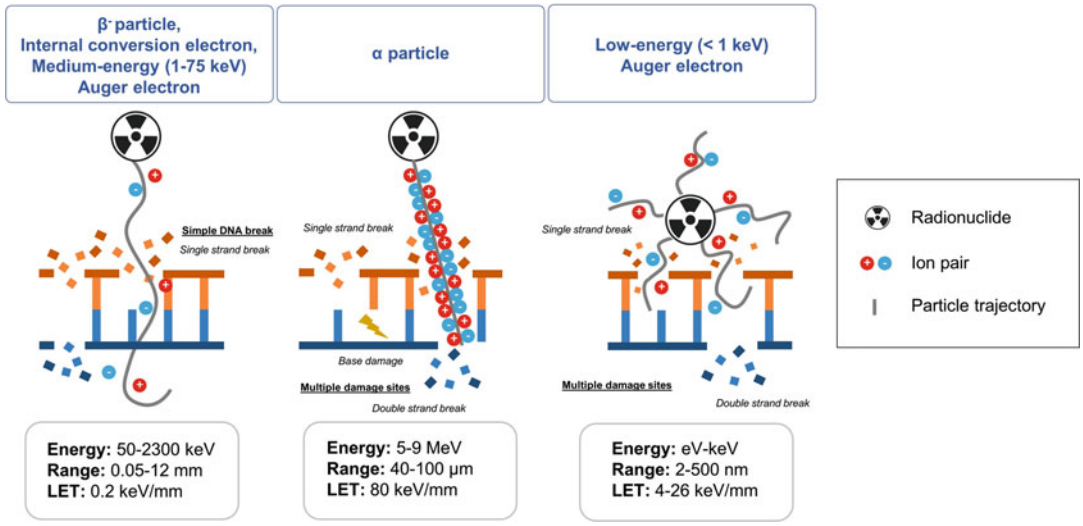

Fig. 5.2 A comparison of the energies, particle ranges and linear energy transfers of α-particles, β-particles and Auger electrons

radionuclides are generally more complex and composed of different types of radiation. Indeed, radionuclides can emit a broad range of particles, including α-particles (i.e. helium nuclei), electrons (β^- particles, internal conversion electrons [ICEs] and AEs), γ-rays and X-rays (Fig. 5.2). Generally, the 'category' of the emitter is determined by its predominant type of cytotoxic or genotoxic radiation. An important parameter for describing and classify radiation is linear energy transfer (LET), which is the average energy released per unit distance travelled by the particle. LET is an average value calculated by assuming a straight path like that of α particles (Fig. 5.2). However, for electrons, the range will be considered rather than the actual path. A distinction is generally made between low (~0.2 keV/µm) and high (50–230 keV/µm) LET particles (Fig. 5.2). In terms of their biological effects, high LET particles such as α-particles (and to some extent AEs) are more harmful than low LET electrons (β-particles or ICE) (Fig. 5.2). To round out the story, γ- or X-rays (used in EBRT) only have a therapeutic role when their number is high enough to create a significant probability that they will interact with biological tissues.

β^--particles, ICEs and AEs are electrons that differ in their origin and energy. β^--particles originate in the nucleus and can reach energies on the order of MeVs (and, consequently, ranges of cm in tissues) (Fig. 5.2). ICEs, in contrast, are monoenergetic electrons ejected from electronic shells outside the nucleus. AEs are also ejected from electronic shells, but their energy comes from the transition of electrons between two atomic shells following the electron capture of ICE processes. Although some AEs can have maximal energies of tens of keV (e.g. 78.2 keV and maximal range of 87 µm for ^{195m}Pt), most AEs have very low energy (<1 keV) that is deposited over distances <500 nm in tissues (Fig. 5.2). Moreover, AEs are emitted in cascades that create a variable number of electrons. Because of their very low energy, AEs can deposit massive amounts of energy in small volumes: up to 10^9 Gy in a 40 nm diameter sphere. While it is true that both β-particles and ICEs will behave like AEs at the end of their tracks, only one of the former is usually emitted per decay compared to up to 35 AEs. As a result, neither β-particles nor ICEs are likely to be as cytotoxic as their AE counterparts.

In RPT, radionuclides are referred as AE-emitters depending on the number of AEs they emit per decay as well as whether the other radiation types associated with their decay could reduce the benefit of their emitted AEs. Due to the volume effects previously defined in the introduction and the lack of cross-fire irradiation (due to their short range), AE-emitters must be administered in far higher activities than β-emitters. So far, there is no consensus on what yield of AEs is required to have a 'significant' therapeutic effect. However, since iodine-125 has long been the reference AE-emitter with 20–23 AEs/decay, it is safe to assume that ~20 AEs/decay is a 'reasonable' threshold [10].

In conclusion, the biological effects of α-particles outweigh those of electrons and of gamma-/X-rays. The effects of AEs take precedence over those of other electrons if they are emitted in high numbers near radiation-sensitive targets (e.g. nuclear DNA, cell membrane, mitochondria).

5.3.1.2 Physical Interactions with Biological Matter

One general principle of physical interactions is that as charged particles interact with matter, their energy decreases, and the probability of their interactions with traversed matter increases. α-Particles, β-particles, ICEs and AEs emitted by radionuclides are all charged particles that will interact with matter according to electrostatic collisions, leading to ionizations and excitations of atoms constituting the matter. Consequently, electrons ejected during ionization processes (called secondary electrons) can in turn lead to a cascade of ionizations/excitations within the molecules with which they collide. This leads to the formation of clusters of ionizations before the electrons are finally stopped.

Beyond their nature and energy, the range and ionization power of particles must also be considered. The standard metric for this discussion is LET. The more the particle interacts with matter, the shorter its path, and the higher its LET. α-Particles are heavy and charged and thus strongly interact with matter such that their linear range in tissue is about 45–100 μm (Fig. 5.2). β-Particles and ICEs, in contrast, are light particles that produce fewer ionizations/excitations per μm; their range can reach up to 12,000 μm. AEs have variable energies (few eV to tens of keV), and those having the highest energies can have a range similar to that of α-particles (e.g. 76 μm for AE emitted by ^{195m}Pt) but a low LET. Indeed, AEs with energies above 1 keV typically produce sparse and isolated ionizations and behave like low LET particles, while AEs with energies below 1 keV interact more with matter and produce dense ionizations (Fig. 5.2). Therefore, those low-energy (< 1 keV) AEs have a higher LET (4–26 keV/μm) over a short distance (< 500 nm). It is worth noting that while α-particles and low-energy AEs are both considered to have high LET, the cytotoxicity of AEs is only observed if they are emitted in the vicinity of sensitive subcellular targets. This is not a problem for α particles, which have a longer range than low-energy AEs and can reach targets at a distance greater than several cell diameters.

The track structure and energy deposition of these particles have been simulated using Monte Carlo approaches. For low-LET particles – i.e. β-particles, γ-rays, X-rays and high-energy AEs – sparse ionizations are produced in a rather large volume, and the energy deposition is somewhat homogenous on the cellular scale [11]. Conversely, high-LET particles (i.e. α-particles) produce high density ionizations along their linear track with little ionization farther afield. This, naturally, renders their energy deposition more heterogeneous. It is generally considered that 1000 sparse tracks are produced per Gy of absorbed low-LET radiation, while a mean number of 4 α-particle tracks is enough to deliver the same dose (Fig. 5.1).

5.3.2 Chemical Steps

The ionization and excitation of molecules described above leads to the breaking of chemical bonds between atoms and to the generation of free radicals. Two types of substrate molecules in cells are considered; on the one hand water, and on the other hand all the other cellular constituents.

5.3.2.1 Indirect Effects

In living beings, water is considered the first target of radiation. The radiolysis of water – generally referred as an 'indirect effect' of radiation – leads to the production of reactive oxygen species (ROS) including hydroxyl radicals, superoxide and hydrogen peroxide [2]. Hydroxyl radicals are exceptionally reactive and are thus responsible for most of the DNA damage [12, 13]. However, $HO^{\bullet}$ has a very short life, reacts within a few nm range from its origin, and thus cannot be transmitted to neighbouring cells. H_2O_2; however, can diffuse through the cell membrane. Because radiation-induced ROS are similar to those endogenously produced, they can be neutralized by the natural enzymatic and chemical antioxidant defences of the cell such as catalase, glutathione peroxidase, superoxide dismutase, glutathione, vitamin E and thioredoxin [14].

5.3.2.2 Direct Effects

In addition to the radiolysis of water, charged particles can directly ionize or excite biomolecules such as lipids, proteins and nucleic acids [15]. These so-called 'direct effects' are expected to predominate with high-LET particles because the high density of radicals produced from water leads to their recombination and thus the abrogation of indirect effects. That said, the situation might not be quite so straightforward, since radical scavengers or antioxidant enzymes have been shown to reduce the cytotoxic effects of high LET particles, indicating that radicals generated from water could be involved too. This could be explained by the fact that the effects of high LET particles result both from targeted effects (involving direct ionization of cellular compounds) and from non-targeted (secondary) effects observed in adjacent cells that would involve free radical mediated mechanisms.

5.3.2.3 Oxygen Effect

Oxygen was identified very early on as an important modulator of radiation response, particularly in the context of the radioresistance of poorly vascularized large tumours. Indeed, the radiosensitizing effect of oxygen has been known since the 1950s [16, 17]. This can be observed using clonogenic assays in which cells exposed to radiation in the presence of oxygen show an increased response. Subsequently, the oxygen enhancement ratio (OER) was introduced to quantify the radiosensitizing effects of oxygen. The OER is the ratio between the dose required to produce a given effect in the presence and absence of oxygen. At the molecular level, oxygen interacts with radiation-induced radicals to produce peroxyl radicals, thereby preventing the recombination of radicals that would decrease radiation cytotoxicity. For example, the yield of DNA lesions upon low LET irradiation was shown to decrease at low oxygen concentration. Low oxygen concentrations also increase the lifetime of radicals that can recombine or interact with radical scavengers. Because α-particles mainly act via direct effects, the concentration of oxygen within a tissue has only a weak influence on their effects; put differently, with α-particles, an OER is typically not observed. However, the bystander effects associated with α-particle irradiation *do* involve radical species, so some dependence on oxygen concentrations is inevitable.

5.3.2.4 Imaging Key Chemical Features: Oxygen and pH

5.3.2.4.1 Oxygen

Nuclear imaging probes capable of delineating tumour oxygenation levels could be particularly valuable in RPT for identifying tumours that are more (or less) likely to response to treatment. Not surprisingly, several probes have been developed and evaluated in a variety of contexts (Fig. 5.6a).

Hypoxia-targeted radiotracers have been explored in the context of EBRT. The most studied PET tracers for hypoxia are ^{18}F-labeled derivatives of 2-nitroimidazole. First developed as radiosensitizers for hypoxic cells, nitroimidazoles undergo an intracellular six-electron reduction in hypoxic cells, leading to the formation of a highly reactive intermediate that binds to macromolecules and traps the radiotracer within cells. ^{18}F-Fluoromisonidazole ([^{18}F]F-MISO), for example, was used in head-and-neck cancer patients to monitor tumour hypoxia and predict treatment outcome before and during

chemo-radiotherapy [18]. Tumour hypoxic sub-volume was shown to decrease in 64% of patients at week 2 post-treatment and in 80% of patients at week 5 post-treatment compared to the baseline scan (i.e. scan performed before the treatment initiation). Moreover, an analysis of 130 radiomic parameters allowed the identification of predictive features. Among them, 35 were able to predict treatment outcome at week 2, and the predictive value of 18 of them was confirmed at week 5. For example, low grey-level zone emphasis (LGZE), a texture feature that quantifies tracer distribution heterogeneity by emphasizing regions with low concentration, was able to differentiate between patients with and without local recurrence. While [^{18}F]F-MISO is the most commonly used hypoxia PET tracer, its high lipophilicity and slow passive diffusion result in relatively low tumour uptake and moderate contrast at best. Therefore, a second generation of nitroimidazole derivatives have been developed – e.g. ^{18}F-[1-(5-fluoro-5-deoxy-α-D-arabinofuranosyl)-2-nitroimidazole)] [^{18}F]F-FAZA – which have displayed enhanced hydrophilicity and improved signal-to-noise contrast ratios in clinical studies.

Another widely studied radiotracer for the imaging of hypoxia is radiocopper-labelled diacetyl-bis(N4-methylthiosemicarbazone) (ATSM). The mechanism of this radioligand's specific accumulation in hypoxic cells remains controversial. Briefly, it is believed that Cu(II)-ATSM diffuses rapidly into cells due to its high membrane permeability and low redox potential. Once internalized, Cu(II)-ATSM is reduced to Cu (I)-ATSM by microsomal and cytosolic enzymes including NADH/NADPH. Under normoxic conditions, Cu(I)-ATSM is reversibly oxidized back to Cu(II)-ATSM and diffuses out of the cell. But under hypoxic conditions, Cu(I)-ATSM is retained within the cell, upon which Cu (I) dissociates from the ligand and remains trapped. [^{60}Cu]Cu-ATSM was evaluated in clinical trials as a predictor of chemoradiotherapy response in patients with cervical cancer and rectal carcinomas [19, 20]. In both studies, patients with high tumour-to-muscle activity concentration ratios that indicated highly hypoxic tumours exhibited poorer survival than those with lower ratios and thus more normoxic tumours. More recently, [^{64}Cu]Cu-ATSM was found to predict the efficacy of carbon ion radiotherapy [21]. More specifically, the in vitro uptake of [^{64}Cu]Cu-ATSM in different cell lines correlated to the relative biological effectiveness (RBE) of carbon ions over X-rays: high RBE cell lines showed greater uptake of [^{64}Cu]Cu-ATSM. This observation was later confirmed in mice xenografted with high and low RBE cell lines.

Finally, one can also highlight hypoxia via the targeted imaging of endogenous markers such as carbonic anhydrase IX (CA-IX) or hypoxia-inducible factor 1-alpha (HIF-1α) [22–24]. Ultimately, despite the promising results shown by these tracers in the context of EBRT and carbon ion radiotherapy, there have yet to be any clinical studies in which hypoxia-targeted probes have been used as theranostic imaging agents for RPT.

5.3.2.4.2 pH Imaging

The pH of a tissue is intimately related to its oxygen concentration, yet pH has not received much attention in the context of radiotherapy. Most normal tissues maintain a stable extracellular pH of around 7.4, while tumours typically have an acidic microenvironment (5.6–6.8). This phenomenon is connected to the increased anaerobic glycolysis (fermentation) of tumours known as the Warburg effect. The Warburg effect is associated with the breakdown of glucose into pyruvate which is in turn converted into lactate by lactate dehydrogenase. This process leads to the expulsion of lactate by monocarboxylate transporters and contributes to the acidification of the microenvironment. An acidic microenvironment is indicative of metabolically aggressive cancer cells and can also be associated with the inhibition of the anti-tumour immune response.

Several recent studies have reinforced the ties between tissue pH and the effects of irradiation. For example, the pH of irradiated skin (7.0 ± 0.3) has been shown to differ from non-irradiated skin (6.5 ± 0.2) [25]. In this study, the authors highlighted that a high pH (7.5 ± 0.3) combined with a low oxygen saturation in irradiated wounds created an unfavourable environment for efficient

wound healing post-radiation. Finally, pH has also been shown to be involved in the gene regulation in irradiated cells. Notably, an acidic microenvironment was shown to enhance the radiation-induced expression of p53 [26]. Altogether, pH modulation remains underinvestigated in the context of (targeted) radiotherapy, and molecular imaging could offer a non-invasive approach to evaluate this physiochemical parameter (Fig. 5.6a).

In a recent study, Pereira et al. showed that external beam radiation activates the sodium/hydrogen exchanger isoform 1 (NHE1) upon radiation-induced glycolytic upregulation [27]. The activation of NHE1 leads to a reversal of the plasma membrane gradient, which in turn results in an alkaline intracellular pH and an acidic extracellular pH. In this same study, Pereira et al. validated the use of a radiolabelled peptide capable of selectively inserting into the membrane of cells under low pH conditions (pHLIP) for monitoring changes in the pH of the extracellular microenvironment following radiotherapy in mice bearing orthotopic pancreatic ductal adenocarcinoma xenografts [27]. The radiotracer – [^{67}Ga]Ga-NO2A-cysVar3 – produced an activity concentration of 8.6 ± 0.7% IA/g in irradiated tumours compared to 3.6 ± 1.9%IA/g in non-irradiated control animals. This study highlights the potential of pH-sensitive molecular probes for the non-invasive assessment of response to radiotherapy.

5.3.3 Molecular Radiobiological Effects

5.3.3.1 DNA

All cellular substrates interact with low- and high-LET radiation, but nuclear DNA has long been identified as the main target because damage DNA is directly related to oncogenic transformation or cell death [28]. For example, hydroxyl radicals produced via the radiolysis of water can produce SSBs by reacting with the sugar or phosphate groups within the DNA backbone. The yield per cell and per Gy of DNA lesions in mammalian cells exposed to EBRT was found to be about 40 DSBs, 1000 SSBs, ~10,000 base modifications and 150 protein DNA crosslinks [11, 29].

If unrepaired or mis-repaired DSBs are the most deleterious form of DNA damage and can be involved in creating both genomic instability and chromosomal aberrations. Persistent DNA damage is also a hallmark of senescence. In EBRT, lesions can be repaired after treatment, and the repair of DNA lesions has been identified as a crucial parameter for radiosensitivity. In RPT, the issue of DNA repair is complicated because the low dose rate means that DNA lesions are repaired while new ones are being produced. Several studies have investigated the yield of DNA damage in vitro as well as in blood cells of patients treated with ^{131}I or [^{223}Ra]$RaCl_2$. However, no relationship could be established between the absorbed dose to the blood and the level of DNA DSBs in blood cells. Furthermore, while the activity in the blood decreased over time, the number of radiation-induced lesions per nucleus and per absorbed dose rate increased over time, suggesting a slowing down of DNA repair or, on the contrary, increased de novo formation [30–34]. Moreover, high LET radiation can produce several DNA modifications at the same site, referred to as 'multiple damage sites' or 'clustered DNA lesions' (MDS, defined as 2+ modifications per turn) (Fig. 5.2) [35–40]. These can include base damage, SSBs and DSBs. MDS cannot be measured by simple methods, and their nature makes them difficult to identify and classify. Due to an increased probability of radical recombination, the number of DNA lesions per dose unit (Gy) decreases when radiation LET rises. However, the probability of MDSs increases with increasing LET [37]. Whether AEs can produce complex DNA lesions will depend on the proximity of the emitter to the DNA, with the highest probability occurring when the radionuclide is incorporated into the DNA itself.

5.3.3.1.1 A Brief Overview of DNA Repair

DNA lesions are continuously produced in cells as the result of endogenous oxidative stress and of errors during DNA replication. As irradiated cells

are generally distributed in the different phases of the cell cycle, the presence of DNA lesions will lead to cell cycle arrest in G1 or G2/M-phase cells or to replication fork progression stalling in S-phase cells. For example, endogenous oxidative lesions (e.g. thymine glycols) on the most prominent oxidized bases in irradiated cells may hinder replication fork progression and generate DNA breaks.

Several DNA Damage Repair (DDR) Pathways

DNA lesions can be repaired by: (i) base excision repair (BER) for base damage, abasic sites and DNA single-strand breaks (SSBs); (ii) nucleotide excision repair (NER) for SSBs and DNA adducts; (iii) mismatch repair for base mismatches, small insertions and deletions and (iv) nonhomologous end-joining (NHEJ) or homologous recombination repair (HRR) for DNA double-strand breaks (DSBs) and crosslinks. Several homologous recombination pathways exist [41]. The major one is the error-free 'synthesis-dependent strand annealing' pathway that implicates RAD51 filaments (detailed below). The presence of single-strand DNA tails – as observed, for example, during DNA synthesis at replication forks, in telomeres or during NER – is not considered by the cell to be a 'normal' situation. Therefore, their presence/absence during the repair of DSBs is a key determinant in the choice between NHEJ and HRR.

Alternative DSB repair mechanisms can be involved when NHEJ and HRR do not operate. The first one is single strand annealing, an error-prone RAD51-independent pathway that joins two homologous 3′-ssDNA ends through annealing. Alternative end homology joining, or microhomology-mediated end joining, also uses 3′-ssDNA, like NHEJ but without NHEJ factors. Finally break-induced replication is involved when there is only one DSB end in RAD51-dependent mechanisms.

Considering now NHEJ, the system is also called 'classical' NHEJ (cNHEJ). It is an error-prone system that requires minimal sequence homology and rapidly joins two DNA ends. Conversely, the error-free HRR mechanism is slower and requires large sequence homology between the broken DNA and the donor DNA molecule, such as a sister chromatid in duplicated DNA [42].

From DNA Damage Recognition to DNA Repair

After DNA lesion recognition and the initiation of a cellular signalling cascade to promote DDR, cell cycle progression is blocked to facilitate DNA repair. For the recognition step, DNA DSBs are detected by the MRE11–RAD50–NBS1 (MRN) and Ku70/Ku80/DNA-PKcs (DNA-PK) complexes [43, 44]. This triggers the DDR through the recruitment and activation of the two major surveillance proteins belonging to the phosphatidylinositol-3-kinase (PI3K)-like kinase family: the serine/threonine protein kinase ataxia telangiectasia mutated (ATM; the main sensor of DNA damage), ATM- and Rad3-related (ATR) and DNA-dependent protein kinase (DNA-PK) [45–47] (Figs. 5.1 and 5.3).

ATR recognizes DSBs and is primarily involved in DNA DSB repair via HRR because it requires duplicated DNA. It occurs in S-phase cells with stalled replication forks or after the G2 phase. ATR recruitment requires ssDNA, for instance obtained after nuclease activation by ATM. Thus, ATR intervenes after ATM action and can in turn phosphorylate proteins, such as checkpoint kinase 1 (CHK1; essential for the intra-S and G2-M checkpoint response) and also BRCA1 to trigger HRR [46].

ATM full activation requires non-resected DNA ends. Its activation leads to the dissociation of ATM homodimers into monomers that phosphorylate and activate downstream protein kinases. These molecules act as transducers and effectors and phosphorylate their own substrate (s). Among them, the core Ku70 and Ku80 proteins (also known as XRCC6–XRCC5) bind to the ends of DNA DSBs before recruiting DNA-dependent protein kinase catalytic subunit (DNA-PKcs). This leads to the formation of a large synapse consisting of two DNA molecules brought into close proximity with the assistance of other associated proteins. Then, the two DNA ends are closely aligned into shorter synapses using XRCC4–DNA ligase IV (LIG4), the XRCC4-like factor (XLF) and DNA-PKcs. The

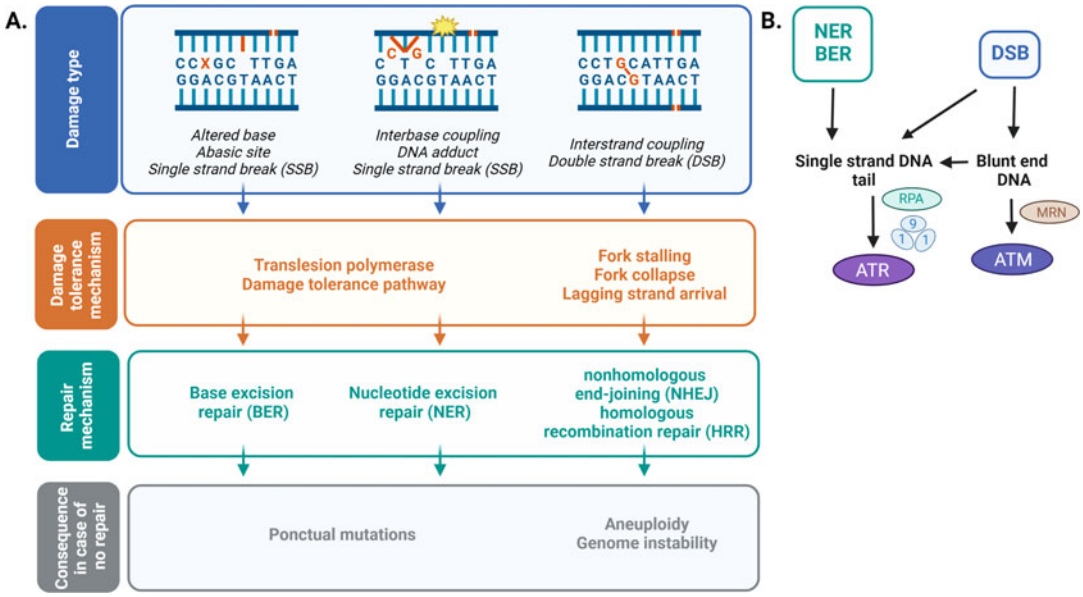

Fig. 5.3 Main radiation-induced DNA damage types. (**a**) Tolerance and repair mechanisms; (**b**) Main damage signalling pathways. Created with BioRender.com

ligation process is terminated by the nuclease Artemis and the DNA polymerases λ and μ. The default engagement of cNHEJ can be avoided by DNA end resection enzymes like MRN.

Phosphorylation of histone H2A (γH2AX) by ATM also is an essential step in the repair process. It allows the remodelling of the chromatin surrounding DSBs and the recruitment of other repair proteins, such as breast cancer type 1 (BRCA1), and p53-binding protein 1 (53BP1) that are involved in HRR promotion and repression, respectively (Fig. 5.1). BRCA1 and 53BP1 participate in the interaction between NBS1 and ATM that is essential for maintaining ATM at DSB sites [47].

Considering now the HRR pathway, it involves the core proteins MRE11, BRCA1 and BRCA2 but also the recombinase RAD51 and replication protein A (RPA). Typically, after Ku70-80 binding to DNA ends, an extended 3′-ssDNA is generated by the 3′-5′ endonuclease resection activity of MRE11, which is part of the MRN complex. This generates ssDNA that is further extended up to 300 nucleotides away from the breakpoint by MRE11 3′−5′ exonuclease activity. Long-range DNA resection is terminated by the 5-3′ exonuclease activity of exonuclease 1 (EXO 1). Then, RPA coats the new ssDNA to prevent pairing with other ssDNA molecules. To allow HRR, RPA must be replaced through the binding of BRCA2 to ssDNA and the formation of RAD51 nucleoprotein filaments. Such filaments are dynamic structures that, in association with BRCA1 and BRCA1-associated RING domain protein 1 (BARD1), participate in RAD51-mediated DNA strand exchange during HRR. It must be noted that homologous recombination deficiency (e.g. in BRCA-mutated tumours) increases sensitivity to PARP inhibitors. PARP recognizes ssDNA and is involved in the repair of SSBs and some base damage. Upon PARP inhibition, DNA breaks accumulate and are converted into DSBs, thus theoretically promoting HRR. In the absence of HRR, the error-prone NHEJ system is involved and contributes to cell killing [48].

DNA End Resection Triggers HRR in the S and G2 Phases

Interestingly, cell cycle-dependent kinase (CDK) activation in cells that enter the S or G2 phase also leads to the phosphorylation and activation of

proteins involved in HRR and of DNA resection proteins required for HRR. Conversely, 53BP1 favours cNHEJ (during the G1 phase) by protecting DSB ends from resection by the DNA end-resection machinery in the G1 phase. 53BP1 is recruited to chromatin via binding to histone H4 monomethylated or demethylated at lysine 20 (H4K20me1 and H4K20me2) and to histone H2A. Therefore, cNHEJ operates throughout the cell cycle, whereas HRR is mainly restricted to the S and G2 phases. DDR is reduced in cells in the late G2 phase and mid-prophase to allow for progression through mitosis.

ATM and ATR Downstream Proteins

ATM phosphorylates and activates downstream protein kinases that act as transducers and effectors and in turn phosphorylate their own substrate(s). For instance, p53 is stabilized by phosphorylation and accumulates to activate other proteins, including p21 that acts on CDKs. CDKs in turn control cell cycle arrest (i.e. G1-S, intra-S and G2-M checkpoints) to give cells time to repair lesions before entering mitosis or to engage in the intrinsic apoptosis process that involves mitochondria and the activation of pro-apoptotic molecules of the BCL2 family (Fig. 5.1).

If the level of damage is too high, p53 can also participate in the induction of apoptosis in the irreversible arrest of proliferation (i.e. senescence). Indeed, p53, which is mutated in 50% of cancers, is one of the many key proteins in the response to RPT. However, p53's role in RPT is not clearly defined because of the heterogeneity of RPT models (radionuclide, vector and cancer type). For example, our group reported that AE-based RPT using ^{125}I-labeled mAbs is p53-independent [49]. Conversely, other authors suggested that the p53-stabilizing peptide VIP116 might potentiate β-RPT [50].

Other ATM substrates include proteins involved in the G1-S (p21), intra-S (FANCD2, BRCA1, SMC1) and G2-M (CHK2) cell cycle arrest, DNA repair poly(ADP-ribose) polymerase 1 (PARP1) and DNA-PK as mentioned above. These factors enable DNA repair through the NHEJ pathway before replication and mitosis.

As patients resistant to prostate-specific membrane antigen (PSMA)-targeted RPT often present mutations in DDR genes, Privé et al. retrospectively investigated 40 tumour biopsies from patients with metastatic castration-resistant prostate cancer (mCRPC) to explore the impact of the DDR on the response to PSMA-targeted RPT. Surprisingly, they *did not* find a correlation between pathogenic DDR gene alterations and higher response to RPT [51]. Conversely, van der Doelen et al. showed in 13 patients with mCRPC treated with [^{225}Ac]Ac-PSMA-617 that higher PSMA expression and DDR gene alterations (determined by immunohistochemistry) were associated with longer patient overall survival [52]. Zhu et al. also reported in one patient with a neuroendocrine tumour that HRR defects may predict treatment response to [^{177}Lu]Lu-DOTATATE [53].

Many preclinical studies have combined RPT with DDR inhibitors. A synergistic effect was observed for a mesothelin-targeted ^{227}Th-labeled radioconjugate and ATR or PARP inhibitors in ovarian cancer xenograft models [54]. PARP inhibitors also were successfully used in combination with α-, β- or AE-RPT in preclinical models [55–59] and in several clinical trials with [^{177}Lu]Lu-DOTATATE, [^{177}Lu]Lu-PSMA-617 and [^{223}Ra]Ra-dichloride.

5.3.3.1.2 Imaging DNA Damage Signalling

The imaging and quantification of DNA damage in cells and tissues has been investigated in the context of aging, mutagenesis, genotoxicity and the response to radiotherapy. With respect to the latter, pulsed field gel electrophoresis (PFGE) and neutral comet assays have historically been used to demonstrate the linear correlation between DNA damage and irradiation dose during acute EBRT. Although very precise, PFGE suffers from a lack of sensitivity and is thus not used anymore. Therefore, alternative approaches allowing for the longitudinal and non-invasive imaging of DNA lesions are desirable. Radiotherapy does not cause DNA damage events – either SDBs or DSBs – in sufficient numbers for direct molecular imaging. Therefore, alternative molecular imaging targets

have been explored, most notably the imaging of DDR proteins such as 53BP1, γH2AX and PARP.

In clinical studies, the quantification of DDR proteins is performed by immunohistochemistry/immunofluorescence on biopsied samples. However, biopsy can only offer the examination of a few tumour sites and can be biased by tumour heterogeneity. Molecular imaging, however, offers the major advantage of in vivo longitudinal studies on a high number of lesions as well as non-targeted healthy organs. Several fluorescence and nuclear imaging approaches for visualizing the DDR have been developed. However, such indirect downstream strategies inevitably raise concerns, for example whether the expression of the detected protein can be correlated to the number of DNA lesions. Furthermore, the presence of these repair markers does not necessarily indicate whether the break repair is complete, and repair foci can also exist in the absence of DSBs [60]. The nature of the DDR as a target also presents several design challenges for radiopharmaceuticals: for example (i) how can probes be driven within cell nucleus when most molecular probes target membrane bound receptors? and (ii) will nuclear probes themselves induce the DDR? Finally, in the specific context of RPT, complex lesions (e.g. MDS) are not properly recognized by DNA sensors (e.g. H2A), which might lead to an underestimation of radiation-induced damages using DDR-targeted probes. The continuous low dose rate of RPT might not induce sufficient DDR to be detected by molecular probes and repair processes will occur while the irradiation is on-going. However, our group showed in colorectal cancer cell lines that DNA damage induced by AE-mediated RPT was effectively detected by the DDR [61]. It is also likely that the biological response to RPT is more complex than after EBRT and will involve signalling pathways between cells that can generate delayed, non-dose-related DNA damage.

Despite the caveats discussed above, two DDR proteins have attracted particular attention as targets for molecular imaging: γH2AX and PARP1 (Fig. 5.4a) [62]. Notably, both SPECT (^{111}In) and PET (^{89}Zr) probes for the in vivo quantification of γH2AX were developed based on an anti-γH2AX antibody. Cornelissen et al. appended a TAT peptide to the antibody in hopes of solving the problem of γH2AX's intranuclear localization [63]. The latter peptide combines cell penetrating properties for transmembrane movement and a nuclear localizing signal (NLS) to bind importins for nucleocytoplasmic trafficking. The authors demonstrated the colocalization of an AF488-anti-γH2AX-TAT with γH2AX foci in cells post-external beam irradiation using confocal microscopy. While the fluorescent probe demonstrated membrane and cytoplasmic uptake 1 h post-irradiation, that accumulation disappeared by 23 h, and a focal nuclear uptake was solely observed. In vivo, the uptake of [^{111}In]In-DTPA-anti-γH2AX-TAT and [^{89}Zr]Zr-DFO-anti-γH2AX-TAT was demonstrated to be proportional to the number of γH2AX foci per cell observed by immunohistochemistry as well as the tumour absorbed dose by external beam radiation (Fig. 5.4b) [63, 64]. As we have noted above, the use of radionuclides to image DDR is a controversial issue, as the ionizing radiation could itself cause further DNA damage and therefore the accumulation of DDR proteins. Thus, it was important for the authors to show that at the specific activity used for imaging (i.e. 0.1–1.0 MBq/μg) with [^{111}In]In-DTPA-anti-γH2AX-TAT and [^{89}Zr]Zr-DFO-anti-γH2AX-TAT did not significantly decrease the cell surviving fraction in a clonogenic assay. However, [^{111}In]In-DTPA-anti-γH2AX-TAT was shown to amplify DNA damage at specific activities >3 MBq/μg [65].

In the context of RPT, [^{111}In]In-DTPA-anti-γH2AX-TAT facilitated the non-invasive visualization of the DNA damage response after [^{177}Lu]Lu-DOTATATE treatment in a preclinical mouse model of pancreatic neuroendocrine cancer [66]. O'Neill et al. underscored the correlations between ^{177}Lu distribution, local absorbed dose heterogeneity and the uptake of [^{111}In]In-DTPA-anti-γH2AX-TAT using a dual isotope SPECT imaging strategy (Fig. 5.4c) [66]. [^{111}In]In-DTPA-anti-γH2AX-TAT showed increased

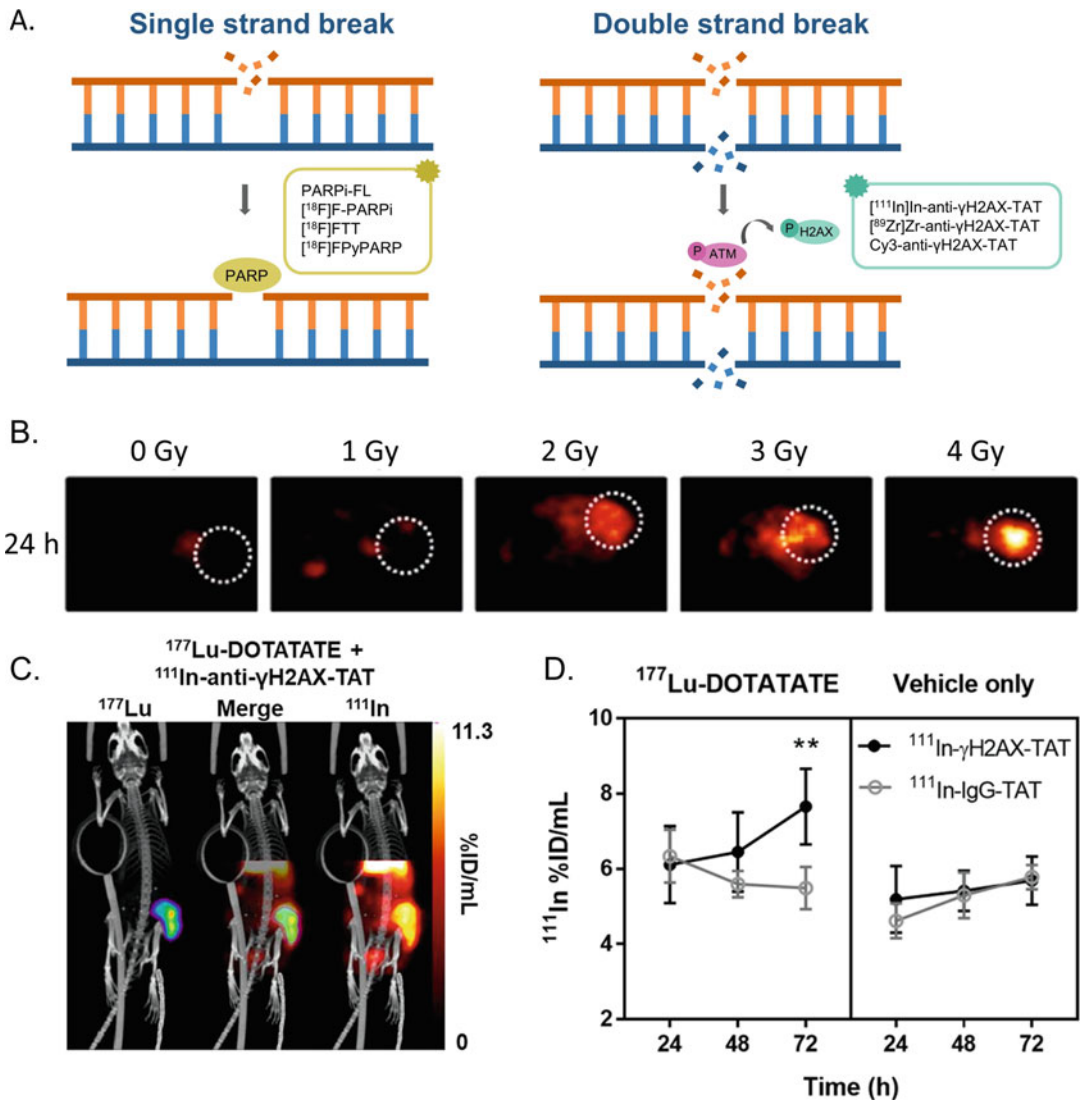

Fig. 5.4 Imaging DNA damage signalling. (**a**) Brief overview of DNA damage biomarkers for molecular imaging and their corresponding targeted molecular probes; (**b**) Transverse SPECT images acquired 24 h after the administration of [^{111}In]In-anti-γH2AX-TAT to mice bearing subcutaneous MDA-MB-468 xenografts that had been subjected to external beam irradiation. The white circles indicate the tumour; (**c**) Dual-isotope SPECT/CT images of mice bearing CA20948 tumours that had been treated with [^{177}Lu]Lu-DOTATATE (20 MBq, 0.33 μg) and were subsequently injected with [^{111}In]In-anti-γH2AX-TAT (5 MBq, 5 μg) 72 h post-RPT. The images were acquired 71 h after the administration of [^{111}In]In-anti-γH2AX-TAT; (**d**) Tumour uptake of [^{111}In]In-anti-γH2AX-TAT and isotype control [^{111}In]In-IgG-TAT at various times after the treatment of mice bearing CA20948 tumours with [^{177}Lu]Lu-DOTATATE (20 MBq, 0.33 μg) or vehicle control

uptake in tumours treated with [^{177}Lu]Lu-DOTATATE compared to animals treated with an isotype control radioimmunoconjugate ([^{111}In]In-DTPA-IgG-TAT) or vehicle alone (Fig. 5.4d). Poty et al. further confirmed the potential of [^{89}Zr]Zr-DFO-anti-γH2AX-TAT for the early monitoring of the DDR following ^{225}Ac- and ^{177}Lu-RPT in a preclinical mouse model of pancreatic adenocarcinoma [67]. However, this study showed no difference in [^{89}Zr]Zr-DFO-anti-γ

H2AX-TAT tumour uptake after α- and β-RPT when the former resulted in prolonged animal survival compared to the latter. This lack of correlation between survival and early DDR highlights that DNA damage is not the sole radiobiology paradigm of merit and that other radiation-induced biological effects (including bystander effects) should be considered.

Both PARPi-FL and [^{18}F]F-PARPi – a fluorescent and ^{18}F-radiolabeled PARP1-targeted small molecule derived from the structure of Olaparib – have been evaluated for the in vivo molecular imaging of PARP1, a DDR protein that is over-expressed in a wide array of cancers. It was shown that the replacement of the cyclopropane group in Olaparib with a BODIPY-based fluorophore or a prosthetic group for ^{18}F-labeling did not affect significantly affect the affinity or specificity of the l small molecule for its target [68]. The preclinical evaluations of both probes in human xenograft models validated their specific accumulation in tumour tissues and led to their clinical translation. PARPi-FL is currently under investigation for the early detection of oral squamous cell carcinoma after topical application [69]. [^{18}F]F-PARPi, in contrast, is currently being evaluated for the imaging of primary and metastatic head and neck cancer lesions [70].

While PARP1 molecular probes have been validated for the imaging of malignant tissue at the preclinical and clinical stage, their application for the evaluation of tumour response to (radio)-therapy remains under-explored. Kossatz et al. used PARPi-FL to visualize a correlation between external irradiation and DNA damage response in a murine model of oral cancer [71]. The probe showed an increased in median radiant efficiency in FaDu tumours within the first 48 h post-external irradiation, $3.2 \pm 0.6 \times 10^8$ for tumour-bearing mice versus $2.3 \pm 0.7 \times 10^8$ for controls. These results were correlated to an increase in PARP1 expression ex vivo, suggesting that PARP1 expression can be measured using PARPi-FL at the whole tumour level. Despite no reports in the context of RPT, this study highlighted the potential of PARPi-FL as a molecular imaging probe of the radiation-induced DNA damage response. Clearly, further studies in the context of RPT are warranted.

5.3.3.2 Lipid Peroxidation and Cell Membrane

DNA is not the only biomolecule subject to radiation-induced damage. Indeed, lipids constituting cellular membranes – specifically their polyunsaturated fatty acids (PUFAs) – can also be oxidized by direct and indirect (i.e. ROS) radiation effects [72]. The resulting carbon-centred radicals participate in chain reactions that can oxidize other PUFAs before leading to lipid-derived metabolites, namely malonedialdehyde (MDA) or 4-hydroxyl-2-nonenal (4HNE). In addition, Haimovitz et al. showed in endothelial cells the role of ceramide as an apoptosis messenger after exposure to high EBRT doses [73]. Ceramide is a sphingolipid that can be formed during the hydrolysis of sphingomyelin (another member of the sphingolipid family) upon the activation of acidic sphingomyelinase by hydroxyl radicals (Fig. 5.1). The coalescence of ceramide into an enriched large domain at the cell surface leads to the activation of signalling pathways involved in cell death or the activation of ion channels. Our group showed that this phenomenon takes place during α- and AE-RPT, suggesting that the local deposition of high levels of energy is required to activate this pathway [72]. In the context of AE-emitters targeting the cell membrane, we demonstrated that signalling pathways turned on by ceramide-enriched large domains activate cyclooxygenase-2 (COX-2) and nitric oxide synthase (NOX), which generate a second wave of ROS and RNS in cells. Those species can then cause further damages to cellular constituents including DNA.

5.3.3.3 Other Extranuclear Targets and Intracellular Communications

Since the first studies focused on the irradiation of the cell cytoplasm [74, 75], the role of this compartment in radiotherapy has been reconsidered. Indeed, the development of α-(external) microbeams that allow for the specific irradiation of subcellular compartments has facilitate the further study of effects of radiation on different cellular compartments. Along these lines, it has

been shown that cytoplasmic irradiation induces oxidative DNA damage and lipid peroxidation, as shown by the increased formation of 4HNE [76–78]. In the cytoplasm, mitochondria – organelles that play a central role in cell metabolism, energy homeostasis and apoptosis – represent up to 25% of the cell volume, which means that the probability that they will be hit by particles is high. Mitochondria contain a circular double-stranded genome (mitochondrial DNA, mtDNA) that encodes proteins and ribosomal RNAs. Reports indicated that the number of mitochondria, their biogenesis and their function were all modified by irradiation with α-particles [79–82]. High-LET irradiation was also shown to cause mitochondrial depolarization and fragmentation [79, 83]. This was accompanied by the participation of the mitochondrial fission regulator, dynamin-related protein 1 (DRP1) in the degradation of dysfunctional mitochondria through induction of autophagy to maintain cellular energy homeostasis. However, mitochondrial fission activated the phosphorylation of the AMP-activated protein kinase (AMPK) and next of ERK1/2 signalling pathways leading to autophagy inhibition and to cell death [84]. Radiation-induced mitochondria damage leading to the dysfunction of respiratory complex I was also observed and created persistent oxidative stress through the increased production of intracellular ROS and further mitochondrial DNA damage. Not surprisingly, the mitochondria are not the only cytoplasmic organelle shown to be impacted by irradiation. Indeed, cells exposed to gadolinium nanoparticles and irradiated have also been shown to contain altered lysosomes (unpublished results). Finally, the expression of tyrosine kinases (e.g. epidermal growth factor receptor), protein kinase C, MAPKs, JNKs, phospholipase C, NF-κB-mediated COX-2 and cytokines as well as the activation of nitric oxide synthase and mechanisms responsible for cytoplasmic Ca^{2+} homeostasis have also been shown to be modulated by radiation (reviewed in [85]).

5.3.3.4 Cellular Cycle Arrest

The activation of the DDR leads to cell cycle arrest of the damaged cells at four specific checkpoints [42, 86, 87]. First, cells irradiated during the G1 phase will stop their progression according to mechanisms under the control of ATM, p53 and p21, preventing entry into S phase. Second, irradiated cells can slow down their progression through S phase with the involvement of ATM, Chk1/Chk12, CDC25A/CDC25C, BRCA1 and BRCA2. Third, irradiated cells can be blocked in early G2 phase to prevent mitosis, a process that is ATM, Chk1/Chk12, CDC25A/CDC25C, BRCA1 and BRCA2 dependent. And fourth, cells are blocked into late G2 (an ATR, Chk1 and CDC25A/CDC25C dependent process).

The progression through the cell cycle is under the control of cyclin-dependent kinases (CDKs) and cyclins that will control those cell cycle checkpoints. In cancer, they are disrupted such that cells can proliferate after the activation of growth-promoting oncogenes, leading to replicative stress and subsequent DNA damage. However, while it is generally thought that cell cycle arrest during EBRT allows the cell more time to repair its DNA, this arrest seems to influence the *quality* of repair rather than the repair itself, as the cell's fundamental radiosensitivity does not seem to be affected. Studies have investigated the role of RPT on cell cycle progression [88–91]. For example, in a lymphoma model, our group showed that cell cycle arrest inhibitors (e.g. MK-1775 and PD-166285 that inhibit G2/M cell cycle progressions) sensitize tumour cells to [^{177}Lu]Lu-lilotomab [89]. This is likely generalizable to tumours with reduced inhibitory CDK1 phosphorylation, such as transformed follicular lymphoma. In ovarian cancer, a ^{177}Lu-labelled variant of the anti-L1CAM antibody chCE7 was also successfully combined with MK1775 [91]. In contrast, others showed that blocking myeloma cells in G2/M phase by combining α-RPT with paclitaxel and doxorubicin led to radiosensitization [90].

5.3.3.5 Cell Proliferation

Despite the induction of DNA damage, cell can repair their damage and continue to proliferate. In the clinic, the assessment of cell proliferation status is largely performed by staining of biopsy

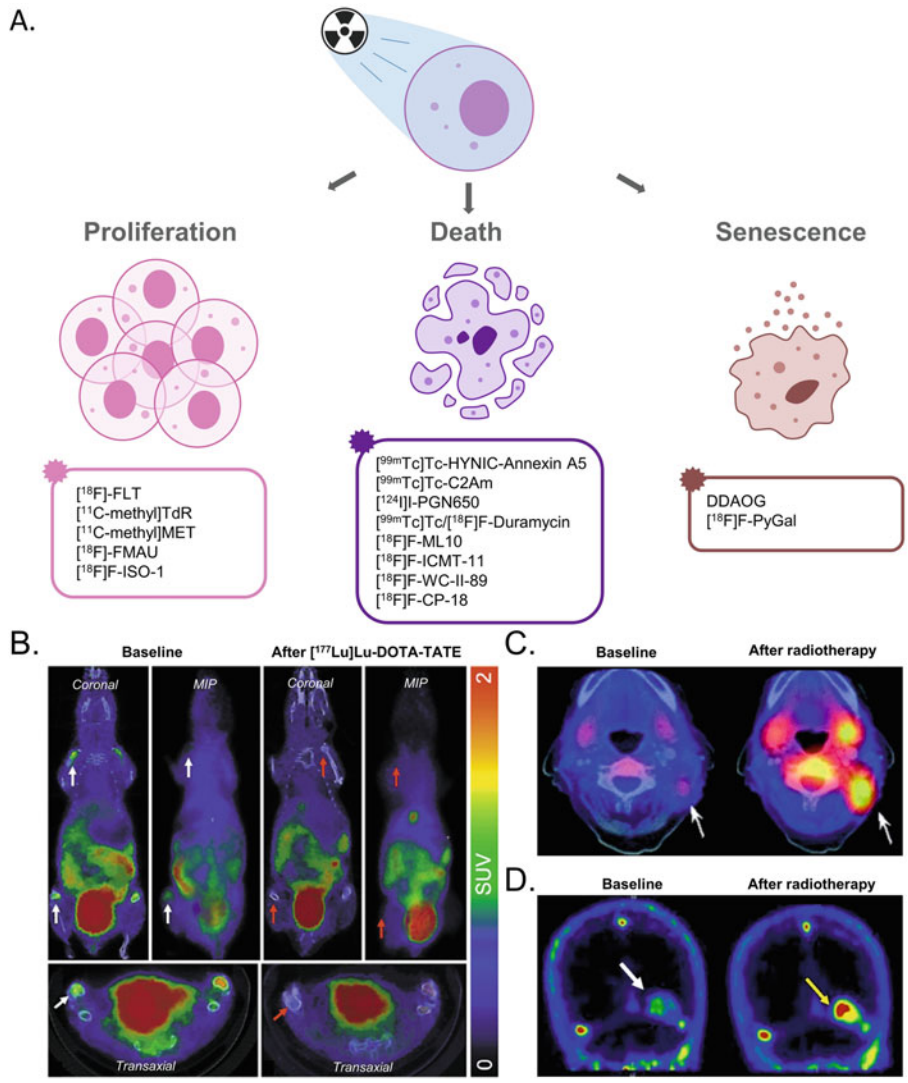

Fig. 5.5 Imaging cell vitality. (**a**) A brief overview of molecular probes for the imaging of cell vital status after irradiation; (**b**) [^{18}F]FLT PET/CT imaging in healthy Balb/cJBomtac mice. [^{18}F]FLT uptake was detected in the bone marrow cavities (white arrows) of the baseline scan. The mice were then treated with 150 MBq of [^{177}Lu]Lu-DOTATATE and imaged again with [^{18}F]FLT. The uptake of [^{18}F]FLT in the marrow cavities (red arrows) was abolished after [^{177}Lu]Lu-DOTATATE therapy, indicating a marked decrease in proliferation. (**c**) [^{99m}Tc]Tc-HYNIC-Annexin A5 SPECT/CT imaging in a 60-year old patient with non-Hodgkin lymphoma. Low-dose radiotherapy induced an increase in [^{99m}Tc]Tc-HYNIC-Annexin A5 uptake in the tumour (white arrow), salivary gland and cervical bone marrow compared to the baseline scan. (**d**) [^{18}F]F-ML-10 PET imaging in a patient with brain metastases treated with whole-brain radiation therapy at 30 Gy in ten daily fractions. While the baseline scan showed a basal apoptotic load, the treated area demonstrated increased [^{18}F]F-ML-10 uptake, reflecting radiation-induced apoptosis

samples for Ki-67, an invasive method that limits the longitudinal follow-up of the proliferative index of multiple tumour lesions. Therefore, the use of molecular imaging probes to assess cell proliferation in vivo could be a useful tool for monitoring the radiobiological response to RPT (Fig. 5.5a).

One established molecular probe for the in vivo assessment of cell proliferation is 3′-deoxy-3′-[^{18}F]fluorothymidine ([^{18}F]-FLT). *In cellulo*, [^{18}F]-FLT is phosphorylated by cytosolic thymidine kinase 1 (TK1) to create FLT-monophosphate and subsequently into the corresponding diphosphate and triphosphates. TK1, a key enzyme in DNA precursor synthesis, is upregulated during cell cycle S phase and is an indicator of active cell proliferation. The substitution of the hydroxyl group at the 5′-end of thymidine with fluorine prevents its binding to DNA. Moreover, once in a triphosphate state, [^{18}F]-FLT remains trapped intracellularly due to its high hydrophilicity. It follows that cancer cells with high proliferative index should exhibit high uptake of [^{18}F]-FLT, and a significant decrease in [^{18}F]-FLT uptake should be observed after therapy.

In preclinical models, Pan et al. used PET/CT to demonstrate that the kinetics of [^{18}F]-FLT were impacted 1-day post-external beam irradiation at doses of 5 Gy and higher [92]. In the clinic, [^{18}F]-FLT uptake in patients with non-small cell lung cancers was shown to correlate with Ki-67 score [93]. Tumour proliferation after curative-intent radiotherapy (46 Gy) in non-small cell lung cancer was further evaluated using [^{18}F]-FLT in 5 patients and compared to [^{18}F]-FDG (metabolism) and [^{18}F]F-MISO (hypoxia). The authors reported a significant decrease in the SUV_{max} of [^{18}F]-FLT in both tumours and nodes, while no statistical differences were observed for [^{18}F]-FDG and [^{18}F]F-MISO [94].

The application of [^{18}F]-FLT imaging to RPT has been very limited. Ahlstedt et al. reported the use of [^{18}F]-FLT to evaluate radiation damage to the bone marrow of mice following treatment with [^{177}Lu]Lu-DOTATATE (Fig. 5.5b) [95]. Compared to mice treated with vehicle alone, mice treated with [^{177}Lu]Lu-DOTATATE showed a marked decrease in [^{18}F]-FLT SUV_{max} from baseline in the different marrow cavities. Despite the lack of tumour-bearing mice, this study highlights the potential of [^{18}F]-FLT to non-invasively image RPT-induced changes in cell proliferation.

5.3.3.6 Cell Death

Cells can die in a variety of ways. The mechanisms of cell death include apoptosis, mitotic death, necrosis, senescence, pyroptosis (an inflammatory form of lytic programmed cell death), ferroptosis (an alteration of the cellular redox metabolism) and anoikis (an extracellular matrix anchorage-independent cell death). DDR proteins play a central role in these outcomes. The diversity and complexity of cell death pathways raise the questions of how cell death can be quantified and whether the different mechanisms can be distinguished. Because radiation-induced cell death can be delayed in time and occur after several rounds of the cell cycle, clonogenic assays were the first gold standard method for measuring cell death [96]. Clonogenic assays describe the ability of cells to form a new colony after several cell divisions (12 days at least). However, the clonogenic survival of senescent cells is equal to zero while the cells are alive and can still secrete factors that can influence the growth or death of neighbouring cells. Clonogenic assays are also limited to in vitro evaluation.

Not surprisingly, imaging probes have been evaluated in this context. Established molecular probes for cell death allow for the monitoring of key cell death features, including cell membrane asymmetry and permeability, changes in mitochondrial transmembrane potential and increased proteolysis (caspase activation). As these phenomena are not restricted to one mechanism of cell death, the imaging probes do not delineate only a single pathway of cell death. Therefore, changes in the uptake of a cell death-targeting probe may result from multiple mechanisms.

The disturbance of cell membrane asymmetry is a feature of apoptosis, pyroptosis, mitotic catastrophe and anoikis. It is characterized by the translocation of phospholipids, specifically phosphatidylethanolamine (PE) and phosphatidylserine (PS), from the inner to the outer leaflet of the cell membrane. Consequently, PE and PS appear as potential target for cell death imaging. Along these lines, it is also important to note that both PE and PS might become accessible during necrosis after integrity of the cell

membrane has been lost. Annexin A5 (also commonly referred as Annexin V) is a protein isolated from the human placenta that has been studied for its Ca^{2+}-dependent binding of negatively charged PS. Derivatives of annexin A5 for nuclear, MR and fluorescence imaging have been developed and evaluated at the preclinical and clinical stages. For example, [^{99m}Tc]Tc-HYNIC-Annexin A5 showed increased uptake in subcutaneous lymphoma xenografts as external beam radiation dose increased [97]. In this same study, the uptake of the SPECT tracer was found to have a linear correlation with the number of apoptotic (i.e. TUNEL-positive) cells.

In the clinic, studies in 33 patients with malignant lymphoma, leukaemia, non-small cell lung cancer and head and neck squamous cell carcinoma reported a marked increase in [^{99m}Tc]Tc-HYNIC-Annexin A5 uptake after radiotherapy compared to baseline in patients with complete or partial response (Fig. 5.5c) [98]. Yet despite promising results, probes based on Annexin A5 probes failed to meet clinical expectations due to their low signal-to-noise ratios related to their slow clearance and high non-specific accumulation in healthy organs especially the liver and kidneys. Moreover, the evaluation of a patient's response to therapy with an Annexin A5-based imaging agent would require multiple scans after treatment, a complex protocol that hampered clinical enthusiasm.

Altered cell membrane permeability is a hallmark of apoptosis. This phenomenon is accompanied by the permanent acidification of the external plasma membrane leaflet and cytosol and an activation of γ-scramblase. The APOSENSE family of compounds have been developed to detect these apoptosis-related alterations. These small molecules possess an amphiphatic (both hydrophilic and hydrophobic) structure that serve as a membrane anchor as well as a charged moiety that prevents the crossing of the healthy cell membrane. Fortuitously, all of the compounds in the group contain an inherently fluorescent dansyl group, and one was labelled with $^{-}$F to create a probe – [^{18}F]F-ML10 – for apoptosis imaging. In ten patients with brain metastases treated with whole-brain irradiation (30 Gy), a significant increase in [^{18}F]F-ML10 uptake was observed in the tumour lesions after radiotherapy (Fig. 5.5d) [99]. This early assessment of response also correlated with later changes in anatomical dimensions as observed by MRI. However, to the best of our knowledge, no evaluation of [^{18}F]F-ML10 in the context of RPT has yet to be reported despite the probe's clear promise.

Cell death is associated with a proteolytic cascade mediated in large part by caspases. Caspase-3 is a key player in apoptosis and has attracted a lot of attention as a target for molecular imaging. However, the design of caspase-targeted probes is a challenge, as caspases are highly homologous and share a high percentage of structural and active site identity. Moreover, any caspase-targeted radiopharmaceutical must be able to cross the plasma membrane because caspases are located in the cytoplasm. For caspase-3 imaging, both small molecule and peptide-based nuclear probes have been evaluated. The small molecule-based radiotracer, [^{18}F]F-ICMT-11, showed higher uptake in chemotherapy-treated tumours compared to controls in murine cancer models [100]. The subsequent clinical investigation of [^{18}F]F-ICMT-11 in healthy volunteers as well as patients with breast and lung cancer revealed a suboptimal mixed renal and hepatobiliary excretion profile that leads to high tumour-to-background activity concentration ratios [101]. Low tumour uptake was reported in cancer patients after first-line chemotherapy, which was imputed to poor apoptosis induction and the heterogeneous response within the tumours [102].

A different imaging agent – [^{18}F]F-CP-18, a caspase-3/-7 substrate based on the pentapeptide DEVDA – demonstrated contrasting results in preclinical evaluations. Specifically, increased uptake was reported in apoptotic tumours in murine cancer models [103]. However, low absolute uptake values were reported for [^{18}F]F-CP-18, raising doubts regarding the level of apoptosis induced and the specificity of the tracer for its target. A phase II clinical trial with [^{18}F]F-CP-18 was initiated in 2012, but this trial was rapidly withdrawn without official explanation. To our knowledge, no evaluation of the radiopharmaceutical has been performed in the context of RPT.

5.3.3.7 Senescence

Cellular senescence is characterized by permanent cell cycle arrest and the activation of a senescence-associated secretory phenotype (SASP). Senescence attracted a great deal of attention in oncology during last decade, and its ambivalent (protective and stimulatory) role has been highlighted in the context of cancer. Recent investigations have led to the addition of senescence to Hanahan's Hallmarks of Cancer in 2022 [104]. While senescence remains underinvestigated in the context of RPT, it is well shown that ionizing radiation from EBRT can induce senescence. Therefore, there is a current need for molecular probes for the non-invasive imaging of cell senescence.

Senescent cells present an overexpression of lysosomal beta-galactosidase, a biomarker that is widely used for the in vitro characterization of senescent cells via histochemical staining. Fluorescent probes for the senescence-associated activation of beta-galactosidase were reported first, most notably a far-red fluorescent beta-galactosidase substrate developed by the Weissleder laboratory [105]. The enzymatic cleavage of this fluorescent probe by beta-galactosidase resulted in a 50 nm red shift that allowed for the specific detection of the cleaved probe against the background fluorescence of the intact probes. In vivo imaging in a model of glioma expressing beta-galactosidase validated the potential of the probe for the real-time in vivo monitoring of beta-galactosidase activity. More recently, a beta-galactosidase-targeting PET radiotracer, [^{18}F]F-PyGal, was evaluated in tumour-bearing mice in which senescence had been induced by chemotherapy [106]. Compared to controls, the uptake of the tracer increased in the chemotherapy-treated animals. Furthermore, the ex vivo comparison of the uptake of the radiotracer (via autoradiography) to the expression of beta-galactosidase (via histochemical staining) showed a strong correlation. These probes should definitely be evaluated in the context of RPT-induced senescence.

5.3.4 The Role of Tissue Microenvironment and Intercellular Communications

5.3.4.1 Bystander and Abscopal Effects

The use of α-microbeam irradiation was a major step forward in understanding the role of intercellular communications, as it allowed for the irradiation of specific cells within a population [107]. More specifically, this technology facilitated the evaluation of both targeted effects in cells traversed by particles as well as so-called non-targeted effects (a.k.a. bystander effects) in neighbouring non-irradiated cells (Fig. 5.1). For example, in one experiment, chromosomal aberrations were observed in 30% of cells, while less than 1% of cells were effectively irradiated [76]. This observation led to a plethora of publications in the field of EBRT. Generally observed at low EBRT doses (<0.5 Gy) when all the cells are not traversed by particles, bystander effects could play a more prominent role in RPT given its lower 'routine' dose-rate irradiation and its heterogeneous dose distribution. To date, bystander effects have been reported after high-LET radiation (α-particles and AEs) but not with β-particles. However, this should be investigated further. Our group reported that RPT-induced bystander effects could be initiated at the cell membrane level (e.g. by a ^{125}I-radiolabelled non-internalizing mAb) through the formation of lipid rafts and also when the radionuclide was located in the DNA (e.g. 5-[^{125}I]I-2'-deoxyuridine, IdUrd) [49, 72, 108]. With α-particles, we showed that 70% of cells were killed by targeted effects, while 30% were killed by bystander effects. Similar proportions of cell killing were obtained with AE-emitters located in the DNA (IdUrd), but these values changed to 15% and 45%, respectively, when AE-emitters were located at the cell membrane level. Finally, bystander effects were observed ex vivo on tumour slices as revealed by immunofluorescence staining in which γH2AX

was shown to be produced over 1 mm from the radiation source as observed using digital autoradiography.

While bystander effects are short range non-targeted effects, systemic effects – also referred as 'abscopal effects' in EBRT – can be observed at longer distances. Abscopal effects are mediated by circulating factors or actors like immune cells. Radiation-induced immunogenic cell death is mediated by the release of danger-associated molecular patterns (DAMPS) like ATP, HMGB1, calreticulin or other molecules like nucleic acids. Through the presence of toll-like receptors, the latter danger signals can next be recognized by phagocytic cells, including macrophages and immature dendritic cells that participate in innate immunity through the generation of a local inflammatory microenvironment. This environment in turn will facilitate the recruitment of other immune cells and the secretion of cytokines, co-stimulating molecules (CD40, CD80, CD86, MHC-I and -II), and chemokine receptors (CCR7) that will drive mature antigen-presenting cells to the lymph nodes where they will cross-present tumour-derived antigens to $CD8^+$ and $CD4^+$ T cells to prime an adaptive immune response [109–111]. Therefore, there has recently been increased interest in the development and evaluation of the radiation-induced anti-tumour immune response.

Several reports in the field of RPT indicate that the immunostimulatory effects of radiation could convert immunologically 'cold' tumours into 'hot' tumours with the hope of increasing the response to immunotherapies [112, 113]. However, so far, RPT parameters that could affect the immune response have not been clearly identified. Radiation nature, absorbed dose, dose rate and dose fractionation may be the major actors, as they will modulate DNA damage and repair and can differentially trigger the cGAS/STING pathway [114–117].

5.3.4.2 Immuno-imaging

Monitoring the immune response in vivo is of major interest not only in the context of RPT but for cancer therapies in general. Several approaches exist for the non-invasive in vivo tracking of immune cells, including the (i) direct labelling of immune cells by in vitro incubation with a radiotracer, (ii) the use of reporter genes and (iii) the use of immunoPET probes directed against immune cell surface receptors (Fig. 5.6). For the sake of brevity, we will only cover a few molecular probes that have been evaluated in the context of the radiation-induced immune response.

$CD8^+$ cytotoxic lymphocytes are key players in the anti-tumour immune response, and a large range of CD8-targeted molecular probes have been developed and evaluated in preclinical and clinical studies. Among them, a $F(ab)'_2$ fragment targeting murine $CD8a^+$ was radiolabelled with copper-64 and evaluated as a tool to evaluate the response of immunocompetent mice bearing colon adenocarcinoma to a combination of CTLA-4 immune checkpoint inhibition and EBRT (Fig. 5.6b) [118]. Notably, the authors reported a significant increase in the tumour-to-heart activity concentration ratios of [^{64}Cu]Cu-NOTA-CD8a in mice receiving EBRT and anti-CTLA-4 therapy as compared to controls. Interestingly, two distinct groups of responding and non-responding mice were observed in the combination therapy cohort in a survival study. A retrospective analysis of [^{64}Cu]Cu-NOTA-CD8a PET imaging highlighted the predictive value of the tracer: the tumour-to-heart activity concentration ratio increased significantly in treated responders compared to treated non-responders and controls.

Tumour-associated macrophages have also drawn the attention of the molecular imaging community, as their number in the tumour microenvironment is known to affect both treatment outcome and cancer prognosis. Therefore, a variety of molecular probes have been explored for the non-invasive imaging of tumour-associated macrophages. For example, Luo et al. developed a dextran-indocyanine green (DN-ICG) nanoprobe for the imaging of tumour-associated macrophages in the second near-infrared window (1000–1700 nm) [119]. The probe was evaluated in a subcutaneous murine model of pancreatic cancer after low-dose radiotherapy (5 Gy) or chemotherapy (zoledronic acid). The fluorescent

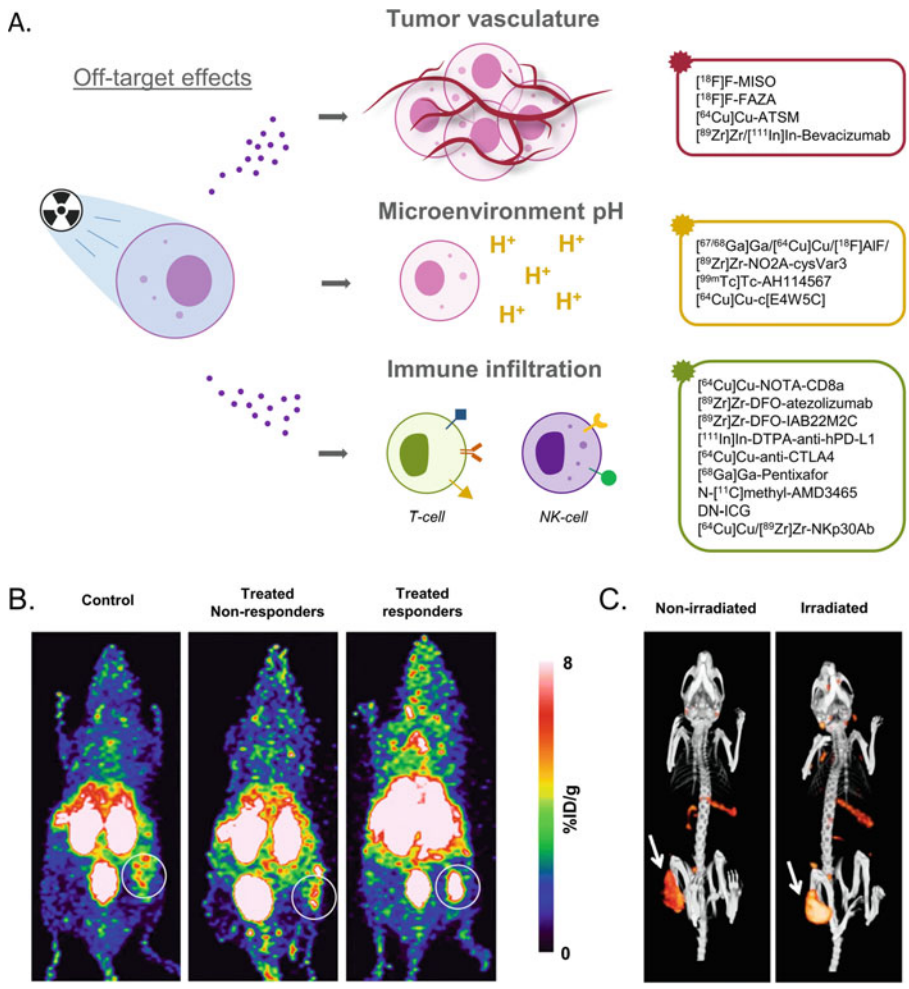

Fig. 5.6 Imaging radiation-induced effects in the tumour microenvironment. (**a**) Examples of radiation-induced off-target effects and their corresponding targeted molecular probes. (**b**) Representative maximum intensity projection of [^{64}Cu]Cu-NOTA-CD8a PET imaging in mice bearing subcutaneous CT26.WT xenografts that had been treated with external beam radiotherapy and anti-CTLA-4 therapy. The mice were retrospectively classified into responders and non-responders to investigate the accuracy of [^{64}Cu]Cu-NOTA-CD8a for therapy monitoring and response prediction. The circles indicate tumours. (**c**) Representative maximum intensity μSPECT/CT projections acquired with [^{111}In]In-anti-mPD-L1 in mice bearing subcutaneous CT26 xenografts that had either been irradiated (10 Gy) or not. The tumours are indicated by arrows

signal in the tumour increased twofold in the case of low-dose radiotherapy and decreased by 50% in the cohort treated with chemotherapy. Importantly, these post-treatment changes were shown to match changes in macrophage infiltration by flow cytometry.

Immune checkpoints are an important component of the immune response, and immune checkpoint inhibitors have – to say the least – garnered a great deal of attention in oncology over the last decade. Programmed death protein ligand 1 (PD-L1) has been found to be upregulated in irradiated tissues. Using a human PD-L1 targeted antibody (atezolizumab) radiolabelled with zirconium-89, Ehlerding et al. assessed the upregulation of PD-L1 in mice bearing subcutaneous lung cancer xenografts receiving two EBRT regimens: 1 × 5 Gy and 5 × 2 Gy [120]. [^{89}Zr]Zr-DFO-atezolizumab enabled the clear visualization of the entire lymph node

network. One day after irradiation, [^{89}Zr]Zr-DFO-atezolizumab produced tumour activity concentrations of 2.4 ± 1.2%IA/g in the 1 × 5 Gy cohort, 4.4 ± 1.5%IA/g in the 5 × 2 Gy and 2.1 ± 0.5%IA/g in the control cohort. Interestingly, this study validated both the potential of the radiotracer to monitor in vivo PD-L1 expression as well as dose fractionation to induce PD-L1 expression.

Since PD-L1 is also expressed by subsets of immune cells, Heskamp et al. validated the potential of [^{111}In]In-DTPA-anti-hPD-L1 for SPECT imaging in tumour-bearing humanized mice [121]. Compared to non-humanized mice, humanized mice exhibited an increased accumulation of [^{111}In]In-DTPA-anti-hPD-L1 in the spleen and lymph nodes. Interestingly, despite high levels of uptake in the lymphoid tissues and the presence of PD-L1-expressing immune cells, the uptake of the tracer in the tumour was not negatively affected by the use of humanized mice. In this same study, the investigators also used SPECT to explore the upregulation of PD-L1 after radiotherapy. Indeed, 24 h after irradiation with 10 Gy, the uptake of [^{111}In]In-DTPA-anti-mPD-L1 was significantly higher in irradiated tumours (26.3 ± 2.0%IA/g) compared to their non-irradiated counterparts (17.1 ± 3.1% IA/g) (Fig. 5.6c).

Finally, the CXCR4-CXCL12 signalling pathway is involved in oncogenesis and the treatment-induced recruitment of CXCR4$^+$ cytotoxic immune cells. Therefore, CXCR4 is also an attractive biomarker for both cancer diagnosis and treatment monitoring. Numerous molecular imaging probes have been developed for the non-invasive imaging of CXCR4 expression. Amongst them, a ^{68}Ga-cyclic pentapeptide known as [^{68}Ga]Ga-Pentixafor has been widely evaluated in clinical trials for the imaging of a broad range of CXCR4-expressing cancers. AMD3100 (Plerixafor®) has also been used as a scaffold for the development of CXCR4-targeted radiopharmaceuticals. To wit, Hartimath et al. validated the use of N-[^{11}C]methyl-AMD3465 for monitoring radiation-induced changes in the expression of CXCR4 by tumours [122]. Tumour-bearing mice were irradiated with a single-fraction 14 Gy dose of external beam radiation. Seven days after irradiation, PET imaging revealed a 2.5-fold higher uptake of the radiotracer in irradiated tumours compared to sham-treated tumours (1.1 ± 0.3%IA/g vs. 0.4 ± 0.1% IA/g, respectively). This study justifies the further evaluation of CXCR4 as an imaging biomarker for the radiation-induced immune response.

5.3.5 Controversial Issues

5.3.5.1 Dose-Response During RPT

One controversial issue of RPT is whether dosimetry is necessary and useful for predicting the efficacy and side effects of RPT. The purpose of radiotherapy is increasing patient survival through local tumour control. The latter is theoretically obtained when all of the tumour's clonogenic cells, which may proliferate and cause recurrence, have been inactivated [123]. The first mathematical models describing the probability of local control referred as 'tumour control probability' (TCP) were introduced one century ago during EBRT. TCP curves describe tumour control progression as a function of tumour absorbed dose and require defining a certain biological endpoint (e.g. based on RECIST criteria). TCP curves show a 'dose threshold' below which no tumour control is observed, followed by an increase in tumour control which correlates with the increasing dose, and finally a tumour control plateau. In EBRT, the absorbed dose is more easily determined as it depends only on the external source of X-rays. Moreover, the field of irradiation is well defined, and dose is considered as homogeneous.

Normal tissue complication probability (NTCP) can also be established for healthy tissues in a manner similar to TCP [124]. As mentioned above, the LQ model was introduced in the 1980s to explain TCP and NTCP. However, RPT faces several challenges. First, absorbed dose determination is not as straightforward as in EBRT, and absorbed doses are still rarely available in either preclinical or clinical models. As a consequence, corresponding alpha and beta values – determined

from dose-response curves – are not available under RPT such that the LQ model has not been validated yet. Another difficulty is that RPT generally aims at treating multiples nodules in metastatic disease. Subsequently, a strong heterogeneity in radiopharmaceutical uptake (and in absorbed doses) can be observed between nodules, even within the same patients. Moreover, for the same absorbed dose, tumour response can be different, suggesting heterogeneity in tumour biology between nodules. Subsequently, the correlation between absorbed dose (and absorbed dose rate) and tumour response can vary dramatically within a single patient from one metastatic lesion to another (unpublished results), suggesting that the relationship between dose and response depends also on other parameters as well. Such observations were also reported by Bodei et al. with respect to the long-term effects of RPT patients with neuroendocrine tumours [125, 126]. For some nodules, an 'inverse dose rate effect' may be also observed, i.e. RPT could be more efficient per Gy than EBRT [127]. It is also likely that continuous low dose rate may be more favourable than high doses and high dose rates for stimulating an immune response [128]. The contribution of non-targeted effects to the final outcome of patients was already highlighted in the literature beginning 20 years ago [129, 130].

In spite of these aspects, some clinical studies including dosimetry (unpublished results) seem to indicate that an absorbed dose threshold, above which tumours don't progress, exists in RPT. This dose threshold now needs to be appreciated regarding toxicity towards healthy tissues.

5.3.5.2 PET Imaging Gold Standard: [^{18}F]F-FDG

[^{18}F]2-fluoro-2-deoxy-D-glucose ([^{18}F]F-FDG) is the most widely used radiotracer in oncology. Because of its high clinical availability and its wide applicability, [^{18}F]F-FDG is the primary molecular imaging probe used in radiation oncology for treatment planning and the evaluation of the efficacy of radiotherapy. [^{18}F]F-FDG is taken up by tumour cells as a result of glucose transport proteins (GLUT1). Once internalized, [^{18}F]F-FDG is phosphorylated into [^{18}F]F-FDG-6-phosphate and is thus metabolically trapped within the cell due to the fluorine substitution. Generally speaking, the uptake of [^{18}F]F-FDG in tumour cells is higher compared to normal tissues due to the high glycolytic rates of tumours. Relative changes in the standard uptake values of [^{18}F]F-FDG (SUVs) are evaluated for the assessment of response to treatment (i.e. chemotherapy, radiotherapy) and the classification of patients into different response categories according to the guidelines of the European Organization for Research and Treatment of Cancer, the National Cancer Institute and the PET Response Criteria in Solid Tumours (PERCIST).

Numerous clinical studies have demonstrated the utility of [^{18}F]F-FDG for the early (during radiotherapy) or late (after radiotherapy) assessment of the metabolic response of tumour tissue in a range of diseases, including lung, head and neck, rectal, oesophageal or cervical cancers [131]. However, the use of [^{18}F]F-FDG to assess response to radiotherapy suffers from a major limitation: the high uptake of [^{18}F]F-FDG in areas of radiation-induced inflammation and the infiltrating macrophages that surrounds the tumour. While the metabolic activity of tumour cells decreases progressively during radiotherapy, this decrease can be counterbalanced by an increase in inflammation. Taken together, this significantly complicates the interpretation of imaging results. Therefore, the timing of the [^{18}F]F-FDG scan is critical. Sufficient tumour cells should be viable in order to extract information, and the surrounding inflammation should be limited. One should also highlight that the quantification of changes in [^{18}F]F-FDG uptake is difficult and sometimes impossible in organs with high baseline metabolic activity such as the brain. To overcome these issues, a shift to more specific biomarkers of radiation-induced biological events – discussed in Sects. 5.2.1, 5.2.2 and 5.2.3 – should be considered. At present, however, this shift remains limited by the availability of the radiotracers.

5.4 The Future of RPT Radiobiology: Imaging and Radiomics Input

Several reports and opinion papers have highlighted the need to specifically investigate the radiobiology of RPT [4, 132]. Beyond preclinical experiments, the collection of data on RECIST and PERCIST criteria, and the analysis of dosimetry data, there is a need to develop the field of clinical RPT radiobiology. This is now possible, as the number of patients treated with RPT is increasing. Clinical samples before and after therapy (i.e. liquid biopsies and tumour samples from patients) together with standard, clinical parameters such as the patient's age, sex, tumour type, tumour grade, previous treatments, lifestyle and environmental factors should be collected and analysed.

Furthermore, in the preceding pages, we have highlighted a broad range of molecular imaging probes that could offer non-invasive approaches to evaluate radiobiology during and after RPT. The collection of images through a broad range of techniques can allow (even in a retrospective manner) for the mining of quantitative features thanks to radiomics. Using mathematical models and artificial intelligence (AI) methods, radiomics entails the exploration of potential associations between imaging features and biological clinical outcomes [133]. The general idea is that standard medical images can provide a large amount of additional information about tumours directly related to their biology [134].

Radiomics could be described in five main steps: image acquisition, post-acquisition image processing, segmentation, radiomic feature extraction and radiomic modelling. However, image pre-processing steps are also needed to homogenize the images in order to reduce noise, enhance quality and facilitate reproducible and comparable radiomic analyses [135]. Segmentation – which consists of contouring regions of interest (ROI) – is a non-negligible step, as radiomic results will differ significantly depending on the ROI delineation (e.g. contouring method or observer). From these ROIs, several hundred radiomic features can extracted, including descriptors of size, shape, volume, intensity distribution (extracted from the histogram) and texture patterns [136]. Texture features refer to a variety of mathematical descriptors that evaluate the grey-level intensity as well as the position of the pixels within the ROI and can thus provide a measure of tumour heterogeneity [137].

The aim of radiomic modelling is to investigate the relationship between image features and an investigated clinical outcome in order to create a model that will provide clinical decision support for diagnosis, prognosis, treatment response prediction or overall survival prediction. This part involves three major steps: feature selection, modelling methodology (training step) and validation [138]. In order to make the model as robust as possible, a hundred input data (i.e. patients or animals), whose investigated outcome is known are required to produce a dataset [139]. This dataset is randomly divided into two cohorts: one for feature selection and training (70%), and the other for validation (30%). The aim of feature selection is to reduce the risk of overfitting by excluding irrelevant or redundant features. Several machine learning algorithms are generally applied to train the model, such as random forests, support vector machines and neural networks. Finally, each model is evaluated using the validation cohort and by measuring the confusion matrix. Ultimately, the model with the best performance is selected.

We strongly believe that the generation of large data banks with biological samples and medical images in tandem with the coalition of researchers and clinicians with a broad range of expertise have the power to drive major breakthroughs in the radiobiology of RPT.

5.5 The Bottom Line

- RPT offers a unique opportunity to irradiate all tumour sites in metastatic disease with low- or high-LET radiation.
- The radiobiology of RPT cannot strictly be extrapolated from the radiobiology of EBRT.

- Non-targeted effects – including short-distance communications (bystander cytotoxicity) and long-distance systemic effects (including immune system activation) – should be considered alongside the effects to targeted tissues.
- Clinical radiobiology using patient data and samples needs to be more deeply and widely explored.
- Molecular imaging probes for the non-invasive monitoring of radiation-induced biological events have already been developed, but only a very limited number have been evaluated in the context of RPT.
- The use of imaging in radiobiology remains under-investigated and is faced by numerous challenges, including (i) the availability of appropriate and relevant radiotracers, (ii) the appropriate timing of follow-up scans, (iii) the accumulation of the radiotracer in areas surrounding the tumour or normal tissues and (iv) poor signal-to-noise ratios.
- The combination of radiomics and artificial intelligence methods may entail the exploration of both preclinical and clinical radiobiology.

Acknowledgements This work was supported by SIRIC Montpellier Cancer Grant INCa_Inserm_DGOS_12553, INCa-Cancéropôle GSO, AVIESAN PCSI (#ASC20025FSA), LABEX MabImprove, Région Occitanie and Fondation ARC pour la Recherche sur le Cancer.

References

1. Herrmann K, Schwaiger M, Lewis JS, Solomon SB, McNeil BJ, Baumann M, et al. Radiotheranostics: a roadmap for future development. Lancet Oncol. 2020;21(3):e146–56.
2. Pouget JP, Lozza C, Deshayes E, Boudousq V, Navarro-Teulon I. Introduction to radiobiology of targeted radionuclide therapy. Front Med (Lausanne). 2015;2:12.
3. Pouget JP, Constanzo J. Revisiting the radiobiology of targeted alpha therapy. Front Med (Lausanne). 2021;8:692436.
4. EANM Radiobiology Working Group, Pouget JP, Konijnenberg M, Eberlein U, Glatting G, Gabina PM, et al. An EANM position paper on advancing radiobiology for shaping the future of nuclear medicine. Eur J Nucl Med Mol Imaging. 2022; https://doi.org/10.1007/s00259-022-05934-2.
5. Holsti LR. Development of clinical radiotherapy since 1896. Acta Oncol. 1995;34(8):995–1003.
6. Puck TT, Marcus PI. Action of X-Rays on mammalian cells. J Exp Med. 1956;103(5):653–66.
7. Turesson I. Radiobiological aspects of continuous low dose-rate irradiation and fractionated high dose-rate irradiation. Radiother Oncol. 1990;19(1):1–15.
8. Van Der Kogel AJ. The dose-rate effect. In: Joiner M, van der Kogel A, editors. Basic clinical radiobiology. London: Hodder Arnold; 2009.
9. Thames HD. Repair kinetics in tissues: alternative models. Radiother Oncol. 1989;14(4):321–7.
10. Ku A, Facca VJ, Cai Z, Reilly RM. Auger electrons for cancer therapy – a review. EJNMMI Radiopharm Chem [Internet]. 2019 [cited 2021 Jun 8];4(1):27. Available from: https://ejnmmipharmchem.springeropen.com/articles/10.1186/s41181-019-0075-2.
11. Goodhead DT. Spatial and temporal distribution of energy. Health Phys [Internet]. 1988 [cited 2021 Jul 6];55(2):231–40. Available from: http://journals.lww.com/00004032-198808000-00015.
12. Halliwell B, Gutteridge JMC. Oxygen toxicity, oxygen radicals, transition metals and disease. Biochem J [Internet]. 1984 [cited 2022 Dec 10];219(1):1–14. Available from: https://portlandpress.com/biochemj/article/219/1/1/15857/Oxygen-toxicity-oxygen-radicals-transition-metals.
13. Cadet J, Delatour T, Douki T, Gasparutto D, Pouget JP, Ravanat JL, et al. Hydroxyl radicals and DNA base damage. Mutat Res. 1999;424(1–2):9–21.
14. Laurent C, Voisin P, Pouget JP. DNA damage in cultured skin microvascular endothelial cells exposed to gamma rays and treated by the combination pentoxifylline and α-tocopherol. Int J Radiat Biol [Internet]. 2006 [cited 2022 Dec 9];82(5):309–21. Available from: http://www.tandfonline.com/doi/full/10.1080/09553000600733150.
15. Cadet J, Douki T, Ravanat JL. One-electron oxidation of DNA and inflammation processes. Nat Chem Biol [Internet]. 2006 [cited 2022 Dec 10];2(7):348–9. Available from: http://www.nature.com/articles/nchembio0706-348.
16. Gray LH, Conger AD, Ebert M, Hornsey S, Scott OCA. The concentration of oxygen dissolved in tissues at the time of irradiation as a factor in radiotherapy. BJR [Internet]. 1953 [cited 2021 Jun 1];26(312):638–48. Available from: http://www.birpublications.org/doi/10.1259/0007-1285-26-312-638.
17. Wright EA, Howard-Flanders P. The influence of oxygen on the radiosensitivity of mammalian tissues. Acta Radiol. 1957;48(1):26–32.
18. Carles M, Fechter T, Grosu AL, Sörensen A, Thomann B, Stoian RG, et al. 18F-FMISO-PET hypoxia monitoring for head-and-neck cancer patients: radiomics analyses predict the outcome of chemoradiotherapy. Cancers (Basel). 2021;13(14):3449.

19. Dietz DW, Dehdashti F, Grigsby PW, Malyapa RS, Myerson RJ, Picus J, et al. Tumor hypoxia detected by positron emission tomography with 60Cu-ATSM as a predictor of response and survival in patients undergoing Neoadjuvant chemoradiotherapy for rectal carcinoma: a pilot study. Dis Colon Rectum. 2008;51(11):1641–8.
20. Dehdashti F, Grigsby PW, Lewis JS, Laforest R, Siegel BA, Welch MJ. Assessing tumor hypoxia in cervical cancer by PET with 60Cu-Labeled Diacetyl-Bis(N4-Methylthiosemicarbazone). J Nucl Med. 2008;49(2):201–5.
21. Nachankar A, Oike T, Hanaoka H, Kanai A, Sato H, Yoshida Y, et al. 64Cu-ATSM predicts efficacy of carbon ion radiotherapy associated with cellular antioxidant capacity. Cancers. 2021;13(24):6159.
22. Huizing FJ, Garousi J, Lok J, Franssen G, Hoeben BAW, Frejd FY, et al. CAIX-targeting radiotracers for hypoxia imaging in head and neck cancer models. Sci Rep. 2019;9(1):18898.
23. Ueda M, Kudo T, Mutou Y, Umeda IO, Miyano A, Ogawa K, et al. Evaluation of [125I]IPOS as a molecular imaging probe for hypoxia-inducible factor-1-active regions in a tumor: comparison among single-photon emission computed tomography/X-ray computed tomography imaging, autoradiography, and immunohistochemistry. Cancer Sci. 2011;102(11):2090–6.
24. Huang Y, Fan J, Li Y, Fu S, Chen Y, Wu J. Imaging of tumor hypoxia with radionuclide-labeled tracers for PET. Front Oncol [Internet]. 2021 [cited 2022 May 13];11. Available from: https://www.frontiersin.org/article/10.3389/fonc.2021.731503.
25. Auerswald S, Schreml S, Meier R, Blancke Soares A, Niyazi M, Marschner S, et al. Wound monitoring of pH and oxygen in patients after radiation therapy. Radiat Oncol. 2019;14:199.
26. Choi EK, Roberts KP, Griffin RJ, Han T, Park HJ, Song CW, et al. Effect of pH on radiation-induced p53 expression. Int J Radiat Oncol Biol Phys. 2004;60(4):1264–71.
27. Pereira PMR, Edwards KJ, Mandleywala K, Carter LM, Escorcia FE, Campesato LF, et al. iNOS regulates the therapeutic response of pancreatic cancer cells to radiotherapy. Cancer Res. 2020;80(8):1681–92.
28. Frankenberg-Schwager M. Review of repair kinetics for DNA damage induced in eukaryotic cells in vitro by ionizing radiation. Radiother Oncol [Internet]. 1989 [cited 2021 Jul 6];14(4):307–20. Available from: https://linkinghub.elsevier.com/retrieve/pii/0167814089901436.
29. Goodhead DT. Initial events in the cellular effects of ionizing radiations: clustered damage in DNA. Int J Radiat Biol [Internet]. 1994 [cited 2021 May 31];65(1):7–17. Available from: http://www.tandfonline.com/doi/full/10.1080/09553009414550021.
30. Signore A, Campagna G, Marinaccio J, de Vitis M, Lauri C, Berardinelli F, et al. Analysis of short term and stable DNA damage in patients with differentiated thyroid cancer treated with ^{131}I in hypothyroidism or with rhTSH for remnant ablation. J Nucl Med [Internet]. 2022 [cited 2022 Aug 31]. Available from: http://jnm.snmjournals.org/lookup/doi/10.2967/jnumed.121.263442.
31. Lassmann M, Hänscheid H, Gassen D, Biko J, Meineke V, Reiners C, et al. In vivo formation of γ-H2AX and 53BP1 DNA repair foci in blood cells after radioiodine therapy of differentiated thyroid cancer. J Nucl Med [Internet]. 2010 [cited 2022 Aug 31];51(8):1318–25. Available from: http://jnm.snmjournals.org/lookup/doi/10.2967/jnumed.109.071357.
32. Schumann S, Scherthan H, Pfestroff K, Schoof S, Pfestroff A, Hartrampf P, et al. DNA damage and repair in peripheral blood mononuclear cells after internal ex vivo irradiation of patient blood with 131I. Eur J Nucl Med Mol Imaging. 2022;49(5):1447–55.
33. Schumann S, Eberlein U, Lapa C, Müller J, Serfling S, Lassmann M, et al. α-Particle-induced DNA damage tracks in peripheral blood mononuclear cells of [223Ra]RaCl2-treated prostate cancer patients. Eur J Nucl Med Mol Imaging [Internet]. 2021 [cited 2022 Aug 31];48(9):2761–70. Available from: https://link.springer.com/10.1007/s00259-020-05170-6.
34. Eberlein U, Scherthan H, Bluemel C, Peper M, Lapa C, Buck AK, et al. DNA damage in peripheral blood lymphocytes of thyroid cancer patients after radioiodine therapy. J Nucl Med [Internet]. 2016 [cited 2022 Aug 31];57(2):173–9. Available from: http://jnm.snmjournals.org/lookup/doi/10.2967/jnumed.115.164814.
35. Lomax EM, Gulston KM, O'Neill P. Chemical aspects of clustered DNA damage induction by ionising radiation. Radiat Protect Dosim [Internet]. 2002 [cited 2021 Mar 3];99(1):63–8. Available from: https://academic.oup.com/rpd/article-lookup/doi/10.1093/oxfordjournals.rpd.a006840.
36. Eccles LJ, O'Neill P, Lomax ME. Delayed repair of radiation induced clustered DNA damage: friend or foe? Mutat Res. 2011;711(1–2):134–41.
37. Pouget JP, Frelon S, Ravanat JL, Testard I, Odin F, Cadet J. Formation of modified DNA bases in cells exposed either to gamma radiation or to high-LET particles. Radiat Res [Internet]. 2002 [cited 2021 May 31];157(5):589–95. Available from: http://www.bioone.org/doi/abs/10.1667/0033-7587%282002%29157%5B0589%3AFOMDBI%5D2.0.CO%3B2.
38. Sasaki MS. Advances in the biophysical and molecular bases of radiation cytogenetics. Int J Radiat Biol [Internet]. 2009 [cited 2022 Dec 9];85(1):26–47. Available from: http://www.tandfonline.com/doi/full/10.1080/09553000802641185.

39. Georgakilas A. Detection of clustered DNA lesions: biological and clinical applications. World J Biol Chem. 2011;2(7):173–6.
40. Sage E, Shikazono N. Radiation-induced clustered DNA lesions: repair and mutagenesis. Free Radic Biol Med. 2017;107:125–35.
41. Amoretti M, Amsler C, Bonomi G, Bouchta A, Bowe P, Carraro C, et al. Production and detection of cold antihydrogen atoms. Nature. 2002;419(6906):456–9.
42. Rothkamm K, Krüger I, Thompson LH, Löbrich M. Pathways of DNA double-strand break repair during the mammalian cell cycle. Mol Cell Biol [Internet]. 2003 [cited 2022 Dec 10];23(16):5706–15. Available from: https://journals.asm.org/doi/10.1128/MCB.23.16.5706-5715.2003.
43. Rothkamm K, Krüger I, Thompson LH, Löbrich M. Pathways of DNA double-strand break repair during the mammalian cell cycle. Mol Cell Biol. 2003;23(16):5706–15.
44. Shibata A, Jeggo P, Löbrich M. The pendulum of the Ku-Ku clock. DNA Repair (Amst). 2018;71:164–71.
45. Shiloh Y, Ziv Y. The ATM protein kinase: regulating the cellular response to genotoxic stress, and more. Nat Rev Mol Cell Biol. 2013;14(4):197–210.
46. Marechal A, Zou L. DNA damage sensing by the ATM and ATR kinases. Cold Spring Harb Perspect Biol [Internet]. 2013 [cited 2022 Oct 10];5(9):a012716. Available from: http://cshperspectives.cshlp.org/lookup/doi/10.1101/cshperspect.a012716.
47. Panier S, Boulton SJ. Double-strand break repair: 53BP1 comes into focus. Nat Rev Mol Cell Biol [Internet]. 2014 [cited 2021 May 29];15(1):7–18. Available from: http://www.nature.com/articles/nrm3719.
48. Lord CJ, Ashworth A. PARP inhibitors: synthetic lethality in the clinic. Science. 2017;355(6330):1152–8.
49. Paillas S, Boudousq V, Piron B, Kersual N, Bardiès M, Chouin N, et al. Apoptosis and p53 are not involved in the anti-tumor efficacy of ^{125}I-labeled monoclonal antibodies targeting the cell membrane. Nucl Med Biol. 2013;40(4):471–80.
50. Lundsten S, Berglund H, Jha P, Krona C, Hariri M, Nelander S, et al. p53-Mediated radiosensitization of 177Lu-DOTATATE in neuroblastoma tumor spheroids. Biomol Ther. 2021;11(11):1695.
51. Privé BM, Slootbeek PHJ, Laarhuis BI, Naga SP, van der Doelen MJ, van Kalmthout LWM, et al. Impact of DNA damage repair defects on response to PSMA radioligand therapy in metastatic castration-resistant prostate cancer. Prostate Cancer Prostatic Dis [Internet]. 2022 [cited 2022 Aug 31];25(1):71–8. Available from: https://www.nature.com/articles/s41391-021-00424-2.
52. van der Doelen MJ, Mehra N, van Oort IM, Looijen-Salamon MG, Janssen MJR, Custers JAE, et al. Clinical outcomes and molecular profiling of advanced metastatic castration-resistant prostate cancer patients treated with 225Ac-PSMA-617 targeted alpha-radiation therapy. Urol Oncol: Semin Orig Investig [Internet]. 2021 [cited 2022 Dec 9];39(10):729.e7–16. Available from: https://linkinghub.elsevier.com/retrieve/pii/S1078143920306311.
53. Zhu M, Sonbol MB, Halfdanarson T, Hobday T, Ahn D, Ma WW, et al. Homologous recombination repair defect may predict treatment response to peptide receptor radionuclide therapy for neuroendocrine tumors. Oncologist [Internet]. 2020 [cited 2022 Dec 9];25(8):e1246–8. Available from: https://academic.oup.com/oncolo/article/25/8/e1246/6443870.
54. Wickstroem K, Hagemann UB, Cruciani V, Wengner AM, Kristian A, Ellingsen C, et al. Synergistic effect of a mesothelin-targeted ^{227} Th conjugate in combination with DNA damage response inhibitors in ovarian cancer xenograft models. J Nucl Med [Internet]. 2019 [cited 2022 Dec 9];60(9):1293–300. Available from: http://jnm.snmjournals.org/lookup/doi/10.2967/jnumed.118.223701.
55. Makvandi M, Lee H, Puentes LN, Reilly SW, Rathi KS, Weng CC, et al. Targeting PARP-1 with alpha-particles is potently cytotoxic to human neuroblastoma in preclinical models. Mol Cancer Ther. 2019;18(7):1195–204.
56. Jannetti SA, Carlucci G, Carney B, Kossatz S, Shenker L, Carter LM, et al. PARP-1–targeted radiotherapy in mouse models of glioblastoma. J Nucl Med. 2018;59(8):1225–33.
57. Fu J, Qiu F, Stolniceanu CR, Yu F, Zang S, Xiang Y, et al. Combined use of ^{177} Lu-DOTATATE peptide receptor radionuclide therapy and fluzoparib for treatment of well-differentiated neuroendocrine tumors: a preclinical study. J Neuroendocrinol [Internet]. 2022 [cited 2022 Dec 9];34(4). Available from: https://onlinelibrary.wiley.com/doi/10.1111/jne.13109.
58. Purohit NK, Shah RG, Adant S, Hoepfner M, Shah GM, Beauregard JM. Potentiation of 177Lu-octreotate peptide receptor radionuclide therapy of human neuroendocrine tumor cells by PARP inhibitor. Oncotarget. 2018;9(37):24693–706.
59. Pirovano G, Jannetti SA, Carter LM, Sadique A, Kossatz S, Guru N, et al. Targeted brain tumor radiotherapy using an auger emitter. Clin Cancer Res. 2020;26(12):2871–81.
60. Atkinson J, Bezak E, Kempson I. Imaging DNA double-strand breaks — are we there yet? Nat Rev Mol Cell Biol [Internet]. 2022 [cited 2022 Aug 31]. Available from: https://www.nature.com/articles/s41580-022-00513-7.
61. Piron B, Paillas S, Boudousq V, Pèlegrin A, Bascoul-Mollevi C, Chouin N, et al. DNA damage-centered signaling pathways are effectively activated during low dose-rate Auger radioimmunotherapy. Nucl Med Biol. 2014;41:e75–83.
62. Knight JC, Koustoulidou S, Cornelissen B. Imaging the DNA damage response with PET and SPECT. Eur J Nucl Med Mol Imaging. 2017;44(6):1065–78.

63. Cornelissen B, Kersemans V, Darbar S, Thompson J, Shah K, Sleeth K, et al. Imaging DNA damage in vivo using gammaH2AX-targeted immunoconjugates. Cancer Res. 2011;71(13):4539–49.
64. Knight JC, Topping C, Mosley M, Kersemans V, Falzone N, Fernández-Varea JM, et al. PET imaging of DNA damage using (89)Zr-labelled anti-γH2AX-TAT immunoconjugates. Eur J Nucl Med Mol Imaging. 2015;42(11):1707–17.
65. Cornelissen B, Darbar S, Kersemans V, Allen D, Falzone N, Barbeau J, et al. Amplification of DNA damage by a γH2AX-targeted radiopharmaceutical. Nucl Med Biol. 2012;39(8):1142–51.
66. O'Neill E, Kersemans V, Allen PD, Terry SYA, Torres JB, Mosley M, et al. Imaging DNA damage repair in vivo following 177Lu-DOTATATE therapy. J Nucl Med [Internet]. 2019 [cited 2022 May 16]. Available from: https://jnm.snmjournals.org/content/early/2019/11/21/jnumed.119.232934.
67. Poty S, Mandleywala K, O'Neill E, Knight JC, Cornelissen B, Lewis JS. 89Zr-PET imaging of DNA double-strand breaks for the early monitoring of response following α- and β-particle radioimmunotherapy in a mouse model of pancreatic ductal adenocarcinoma. Theranostics. 2020;10(13):5802–14.
68. Carney B, Kossatz S, Reiner T. Molecular imaging of PARP. J Nucl Med. 2017;58(7):1025–30.
69. de Souza D, França P, Kossatz S, Brand C, Karassawa Zanoni D, Roberts S, Guru N, et al. A phase I study of a PARP1-targeted topical fluorophore for the detection of oral cancer. Eur J Nucl Med Mol Imaging. 2021;48(11):3618–30.
70. Schöder H, França PDDS, Nakajima R, Burnazi E, Roberts S, Brand C, et al. Safety and feasibility of PARP1/2 imaging with 18F-PARPi in patients with head and neck cancer. Clin Cancer Res. 2020;26(13):3110–6.
71. Kossatz S, Weber WA, Reiner T. Optical imaging of PARP1 in response to radiation in oral squamous cell carcinoma. PLoS One. 2016;11(1):e0147752.
72. Ladjohounlou R, Lozza C, Pichard A, Constanzo J, Karam J, Le Fur P, et al. Drugs that modify cholesterol metabolism alter the p38/JNK-mediated targeted and nontargeted response to alpha and auger radioimmunotherapy. Clin Cancer Res [Internet]. 2019 [cited 2021 Feb 9];25(15):4775–90. Available from: http://clincancerres.aacrjournals.org/lookup/doi/10.1158/1078-0432.CCR-18-3295.
73. Haimovitz-Friedman A, Kan CC, Ehleiter D, Persaud RS, McLoughlin M, Fuks Z, et al. Ionizing radiation acts on cellular membranes to generate ceramide and initiate apoptosis. J Exp Med [Internet]. 1994 [cited 2021 Mar 26];180(2):525–35. Available from: https://rupress.org/jem/article/180/2/525/50763/Ionizing-radiation-acts-on-cellular-membranes-to.
74. Zirkle RE. Radiation biology. In: Hollaender A, editor. The radiobiological importance of linear energy transfer. New York: McGraw-Hill Book Company; 1954. p. 315–50.
75. Munro TR. The relative radiosensitivity of the nucleus and cytoplasm of Chinese hamster fibroblasts. Radiat Res [Internet]. 1970 [cited 2021 Mar 22];42(3):451. Available from: https://www.jstor.org/stable/3572962?origin=crossref.
76. Nagasawa H, Cremesti A, Kolesnick R, Fuks Z, Little JB. Involvement of membrane signaling in the bystander effect in irradiated cells. Cancer Res. 2002;62(9):2531–4.
77. Shao C, Folkard M, Michael BD, Prise KM. Targeted cytoplasmic irradiation induces bystander responses. Proc Natl Acad Sci [Internet]. 2004 [cited 2021 Mar 26];101(37):13495–500. Available from: http://www.pnas.org/cgi/doi/10.1073/pnas.0404930101.
78. Hong M, Xu A, Zhou H, Wu L, Randers-Pehrson G, Santella RM, et al. Mechanism of genotoxicity induced by targeted cytoplasmic irradiation. Br J Cancer [Internet]. 2010 [cited 2021 Mar 31];103(8):1263–8. Available from: http://www.nature.com/articles/6605888.
79. Zhang B, Davidson MM, Zhou H, Wang C, Walker WF, Hei TK. Cytoplasmic irradiation results in mitochondrial dysfunction and DRP1-dependent mitochondrial fission. Cancer Res [Internet]. 2013 [cited 2021 Mar 31];73(22):6700–10. Available from: http://cancerres.aacrjournals.org/lookup/doi/10.1158/0008-5472.CAN-13-1411.
80. Leach JK, Van Tuyle G, Lin PS, Schmidt-Ullrich R, Mikkelsen RB. Ionizing radiation-induced, mitochondria-dependent generation of reactive oxygen/nitrogen. Cancer Res. 2001;61(10):3894–901.
81. Kim JG, Chandrasekaran K, Morgan FW. Mitochondrial dysfunction, persistently elevated levels of reactive oxygen species and radiation-induced genomic instability: a review. Mutagenesis [Internet]. 2006 [cited 2021 Mar 23];21(6):361–7. Available from: https://academic.oup.com/mutage/article-lookup/doi/10.1093/mutage/gel048.
82. Kam WWY, Banati RB. Effects of ionizing radiation on mitochondria. Free Radic Biol Med [Internet]. 2013 [cited 2020 Sep 14];65:607–19. Available from: http://www.sciencedirect.com/science/article/pii/S0891584913003687.
83. Walsh DWM, Siebenwirth C, Greubel C, Ilicic K, Reindl J, Girst S, et al. Live cell imaging of mitochondria following targeted irradiation in situ reveals rapid and highly localized loss of membrane potential. Sci Rep [Internet]. 2017 [cited 2021 Mar 23];7(1):46684. Available from: http://www.nature.com/articles/srep46684.
84. Wu J, Zhang B, Wuu YR, Davidson MM, Hei TK. Targeted cytoplasmic irradiation and autophagy. Mutat Res/Fundam Mol Mech Mutagen [Internet]. 2017 [cited 2021 Mar 23];806:88–97. Available from: https://linkinghub.elsevier.com/retrieve/pii/S0027510716301476.

85. Pouget JP, Georgakilas AG, Ravanat JL. Targeted and off-target (bystander and abscopal) effects of radiation therapy: redox mechanisms and risk/benefit analysis. Antioxid Redox Signal [Internet]. 2018 [cited 2021 Mar 23];29(15):1447–87. Available from: https://www.liebertpub.com/doi/10.1089/ars.2017.7267.
86. Kastan MB, Bartek J. Cell-cycle checkpoints and cancer. Nature [Internet]. 2004 [cited 2021 Jun 1];432(7015):316–23. Available from: http://www.nature.com/articles/nature03097.
87. Otto T, Sicinski P. Cell cycle proteins as promising targets in cancer therapy. Nat Rev Cancer. 2017;17(2):93–115.
88. Suman S, Priya R, Kameswaran M. Induction of different cellular arrest and molecular responses in low EGFR expressing A549 and high EGFR expressing A431 tumor cells treated with various doses of ^{177} Lu-Nimotuzumab. Int J Radiat Biol [Internet]. 2020 [cited 2022 Aug 31];96(9):1144–56. Available from: https://www.tandfonline.com/doi/full/10.1080/09553002.2020.1793012.
89. Pichard A, Marcatili S, Karam J, Constanzo J, Ladjohounlou R, Courteau A, et al. The therapeutic effectiveness of 177Lu-lilotomab in B-cell non-Hodgkin lymphoma involves modulation of G2/M cell cycle arrest. Leukemia [Internet]. 2020 [cited 2021 Jun 2];34(5):1315–28. Available from: http://www.nature.com/articles/s41375-019-0677-4.
90. Supiot S, Gouard S, Charrier J, Apostolidis C, Chatal JF, Barbet J, et al. Mechanisms of cell sensitization to α radioimmunotherapy by doxorubicin or paclitaxel in multiple myeloma cell lines. Clin Cancer Res [Internet]. 2005 [cited 2022 Oct 10];11(19):7047s–52s. Available from: https://aacrjournals.org/clincancerres/article/11/19/7047s/190792/Mechanisms-of-Cell-Sensitization-to.
91. Lindenblatt D, Terraneo N, Pellegrini G, Cohrs S, Spycher PR, Vukovic D, et al. Combination of lutetium-177 labelled anti-L1CAM antibody chCE7 with the clinically relevant protein kinase inhibitor MK1775: a novel combination against human ovarian carcinoma. BMC Cancer [Internet]. 2018 [cited 2022 Dec 9];18(1):922. Available from: https://bmccancer.biomedcentral.com/articles/10.1186/s12885-018-4836-1.
92. Pan MH, Huang SC, Liao YP, Schaue D, Wang CC, Stout DB, et al. FLT-PET imaging of radiation responses in murine tumors. Mol Imaging Biol. 2008;10(6):325–34.
93. Vesselle H, Grierson J, Muzi M, Pugsley JM, Schmidt RA, Rabinowitz P, et al. In vivo validation of 3'deoxy-3'-[(18)F]fluorothymidine ([(18)F]FLT) as a proliferation imaging tracer in humans: correlation of [(18)F]FLT uptake by positron emission tomography with Ki-67 immunohistochemistry and flow cytometry in human lung tumors. Clin Cancer Res. 2002;8(11):3315–23.
94. Vera P, Bohn P, Edet-Sanson A, Salles A, Hapdey S, Gardin I, et al. Simultaneous positron emission tomography (PET) assessment of metabolism with 18F-fluoro-2-deoxy-d-glucose (FDG), proliferation with 18F-fluoro-thymidine (FLT), and hypoxia with 18fluoro-misonidazole (F-miso) before and during radiotherapy in patients with non-small-cell lung cancer (NSCLC): a pilot study. Radiother Oncol. 2011;98(1):109–16.
95. Ahlstedt J, Johansson E, Sydoff M, Karlsson H, Thordarson E, Gram M, et al. Non-Invasive imaging methodologies for assessment of radiation damage to bone marrow and kidneys from peptide receptor radionuclide therapy. Neuroendocrinology. 2020;110(1–2):130–8.
96. Constanzo J, Garcia-Prada CD, Pouget JP. Clonogenic assay to measure bystander cytotoxicity of targeted alpha-particle therapy. In: Methods in cell biology [Internet]. Elsevier; 2022 [cited 2022 Dec 10]. Available from: https://linkinghub.elsevier.com/retrieve/pii/S0091679X22001303.
97. Guo MF, Zhao Y, Tian R, Li L, Guo L, Xu F, et al. In vivo99mTc-HYNIC-annexin V imaging of early tumor apoptosis in mice after single dose irradiation. J Exp Clin Cancer Res. 2009;28(1):136.
98. Kartachova M, Haas RLM, Valdés Olmos RA, Hoebers FJP, van Zandwijk N, Verheij M. In vivo imaging of apoptosis by 99mTc-Annexin V scintigraphy: visual analysis in relation to treatment response. Radiother Oncol. 2004;72(3):333–9.
99. Allen AM, Ben-Ami M, Reshef A, Steinmetz A, Kundel Y, Inbar E, et al. Assessment of response of brain metastases to radiotherapy by PET imaging of apoptosis with ^{18}F-ML-10. Eur J Nucl Med Mol Imaging. 2012;39(9):1400–8.
100. García-Argüello SF, Lopez-Lorenzo B, Cornelissen B, Smith G. Development of [18F]ICMT-11 for imaging caspase-3/7 activity during therapy-induced apoptosis. Cancers (Basel). 2020;12(8):E2191.
101. Challapalli A, Kenny LM, Hallett WA, Kozlowski K, Tomasi G, Gudi M, et al. 18F-ICMT-11, a caspase-3-specific PET tracer for apoptosis: biodistribution and radiation dosimetry. J Nucl Med. 2013;54(9):1551–6.
102. Dubash SR, Merchant S, Heinzmann K, Mauri F, Lavdas I, Inglese M, et al. Clinical translation of [18F]ICMT-11 for measuring chemotherapy-induced caspase 3/7 activation in breast and lung cancer. Eur J Nucl Med Mol Imaging. 2018;45(13):2285–99.
103. Kolb H, Walsh J, Mocharla V, Liang Q, Zhao T, Gomez F, et al. 18F-CP18: A novel DEVD containing peptide substrate for imaging apoptosis via Caspase-3 activity. J Nucl Med. 2011;52(supplement 1):350.
104. Hanahan D. Hallmarks of cancer: new dimensions. Cancer Discov. 2022;12(1):31–46.
105. Tung CH, Zeng Q, Shah K, Kim DE, Schellingerhout D, Weissleder R. In Vivo imaging

of β-Galactosidase activity using far red fluorescent switch. Cancer Res. 2004;64(5):1579–83.
106. Krueger MA, Cotton JM, Zhou B, Wolter K, Schwenck J, Kuehn A, et al. Abstract 1146: [18F] FPyGal: a novel ß-galactosidase specific PET tracer for in vivo imaging of tumor senescence. Cancer Res. 2019;79(13_Supplement):1146.
107. Barberet P, Seznec H. Advances in microbeam technologies and applications to radiation biology: Table 1. Radiat Prot Dosimetry [Internet]. 2015 [cited 2021 Mar 23];166(1–4):182–7. Available from: https://academic.oup.com/rpd/article-lookup/doi/10.1093/rpd/ncv192.
108. Paillas S, Ladjohounlou R, Lozza C, Pichard A, Boudousq V, Jarlier M, et al. Localized irradiation of cell membrane by auger electrons is cytotoxic through oxidative stress-mediated nontargeted effects. Antioxid Redox Signal [Internet]. 2016 [cited 2021 Feb 9];25(8):467–84. Available from: http://www.liebertpub.com/doi/10.1089/ars.2015.6309.
109. Formenti SC, Demaria S. Systemic effects of local radiotherapy. Lancet Oncol 2009 [cited 2022 Dec 10];10(7):718–26. Available from: https://linkinghub.elsevier.com/retrieve/pii/S1470204509700828.
110. Demaria S, Ng B, Devitt ML, Babb JS, Kawashima N, Liebes L, et al. Ionizing radiation inhibition of distant untreated tumors (abscopal effect) is immune mediated. Int J Radiat Oncol Biol Phys. 2004 [cited 2019 Nov 2];58(3):862–70. Available from: https://linkinghub.elsevier.com/retrieve/pii/S0360301603019382.
111. Demaria S, Formenti SC. Role of T lymphocytes in tumor response to radiotherapy. Front Oncol [Internet]. 2012 [cited 2021 Nov 1];2. Available from: http://journal.frontiersin.org/article/10.3389/fonc.2012.00095/abstract.
112. Lejeune P, Cruciani V, Berg-Larsen A, Schlicker A, Mobergslien A, Bartnitzky L, et al. Immunostimulatory effects of targeted thorium-227 conjugates as single agent and in combination with anti-PD-L1 therapy. J Immunother Cancer. 2021;9(10):e002387.
113. Patel RB, Hernandez R, Carlson P, Grudzinski J, Bates AM, Jagodinsky JC, et al. Low-dose targeted radionuclide therapy renders immunologically cold tumors responsive to immune checkpoint blockade. Sci Transl Med [Internet]. 2021 [cited 2021 Oct 23];13(602):eabb3631. Available from: https://www.science.org/doi/10.1126/scitranslmed.abb3631.
114. Constanzo J, Galluzzi L, Pouget JP. Immunostimulatory effects of radioimmunotherapy. J Immunother Cancer [Internet]. 2022 [cited 2022 May 30];10(2):e004403. Available from: https://jitc.bmj.com/lookup/doi/10.1136/jitc-2021-004403.
115. Rodriguez-Ruiz ME, Vitale I, Harrington KJ, Melero I, Galluzzi L. Immunological impact of cell death signaling driven by radiation on the tumor microenvironment. Nat Immunol [Internet]. 2020 [cited 2020 Oct 5];21(2):120–34. Available from: https://www.nature.com/articles/s41590-019-0561-4.
116. Vanpouille-Box C, Demaria S, Formenti SC, Galluzzi L. Cytosolic DNA sensing in organismal tumor control. Cancer Cell [Internet]. 2018 [cited 2021 Jul 5];34(3):361–78. Available from: https://linkinghub.elsevier.com/retrieve/pii/S1535610818302277.
117. Ablasser A, Goldeck M, Cavlar T, Deimling T, Witte G, Röhl I, et al. cGAS produces a 2′-5′-linked cyclic dinucleotide second messenger that activates STING. Nature [Internet]. 2013 [cited 2021 Jul 5];498(7454):380–4. Available from: http://www.nature.com/articles/nature12306.
118. Kristensen LK, Christensen C, Alfsen MZ, Cold S, Nielsen CH, Kjaer A. Monitoring CD8a+ T cell responses to radiotherapy and CTLA-4 blockade using [64Cu]NOTA-CD8a PET imaging. Mol Imaging Biol. 2020;22(4):1021–30.
119. Luo X, Hu D, Gao D, Wang Y, Chen X, Liu X, et al. Metabolizable near-infrared-II nanoprobes for dynamic imaging of deep-seated tumor-associated macrophages in pancreatic cancer. ACS Nano. 2021;15(6):10010–24.
120. Ehlerding EB, Lee HJ, Barnhart TE, Jiang D, Kang L, McNeel DG, et al. Noninvasive imaging and quantification of radiotherapy-induced PD-L1 upregulation with 89Zr–Df–Atezolizumab. Bioconjug Chem. 2019;30(5):1434–41.
121. Heskamp S, Wierstra PJ, Molkenboer-Kuenen JDM, Sandker GW, Thordardottir S, Cany J, et al. PD-L1 microSPECT/CT imaging for longitudinal monitoring of PD-L1 expression in syngeneic and humanized mouse models for cancer. Cancer Immunol Res. 2019;7(1):150–61.
122. Hartimath S, Draghiciu O, Daemen T, Nijman HW, van Waarde A, Dierckx RAJO, et al. Therapy-induced changes in CXCR4 expression in tumor xenografts can be monitored noninvasively with N-[11C]Methyl-AMD3465 PET. Mol Imaging Biol. 2020;22(4):883–90.
123. Zips D. Tumour growth and response to radiation. In: Joiner M, van der Kogel A, editors. Basic clinical radiobiology. London: Hodder Arnold; 2009.
124. Cremonesi M, Ferrari ME, Bodei L, Chiesa C, Sarnelli A, Garibaldi C, et al. Correlation of dose with toxicity and tumour response to 90Y- and 177Lu-PRRT provides the basis for optimization through individualized treatment planning. Eur J Nucl Med Mol Imaging [Internet]. 2018 [cited 2021 Feb 9];45(13):2426–41. Available from: http://link.springer.com/10.1007/s00259-018-4044-x.
125. Bodei L, Kidd M, Paganelli G, Grana CM, Drozdov I, Cremonesi M, et al. Long-term tolerability of PRRT in 807 patients with neuroendocrine

tumours: the value and limitations of clinical factors. Eur J Nucl Med Mol Imaging [Internet]. 2015 [cited 2019 Nov 2];42(1):5–19. Available from: http://link.springer.com/10.1007/s00259-014-2893-5.

126. Bodei L, Kidd M, Baum RP, Modlin IM. PRRT: defining the paradigm shift to achieve standardization and individualization. J Nucl Med [Internet]. 2014 [cited 2022 Dec 11];55(11):1753–6. Available from: http://jnm.snmjournals.org/lookup/doi/10.2967/jnumed.114.143974.
127. Williams JA, Edwards JA, Dillehay LE. Quantitative comparison of radiolabeled antibody therapy and external beam radiotherapy in the treatment of human glioma xenografts. Int J Radiat Oncol Biol Phys [Internet]. 1992 [cited 2022 Dec 10];24(1):111–7. Available from: https://linkinghub.elsevier.com/retrieve/pii/036030169291029M.
128. Herrera FG, Ronet C, Ochoa de Olza M, Barras D, Crespo I, Andreatta M, et al. Low dose radiotherapy reverses tumor immune desertification and resistance to immunotherapy. Cancer Discov [Internet]. 2021 [cited 2021 Oct 29];candisc.0003.2021. Available from: http://cancerdiscovery.aacrjournals.org/lookup/doi/10.1158/2159-8290.CD-21-0003.
129. Bentzen SM. Preventing or reducing late side effects of radiation therapy: radiobiology meets molecular pathology. Nat Rev Cancer. 2006;6(9):702–13.
130. Prise KM, O'Sullivan JM. Radiation-induced bystander signalling in cancer therapy. Nat Rev Cancer [Internet]. 2009 [cited 2021 Apr 8];9(5):351–60. Available from: http://www.nature.com/articles/nrc2603.
131. Jeraj R, Bradshaw T, Simončič U. Molecular imaging to plan radiotherapy and evaluate its efficacy. J Nucl Med. 2015;56(11):1752–65.
132. Terry SYA, Nonnekens J, Aerts A, Baatout S, de Jong M, Cornelissen B, et al. Call to arms: need for radiobiology in molecular radionuclide therapy. Eur J Nucl Med Mol Imaging. 2019;46(8):1588–90.
133. Kumar V, Gu Y, Basu S, Berglund A, Eschrich SA, Schabath MB, et al. Radiomics: the process and the challenges. Magn Reson Imaging. 2012;30(9):1234–48.
134. Gillies RJ, Kinahan PE, Hricak H. Radiomics: images are more than pictures, they are data. Radiology. 2016;278(2):563–77.
135. Hatt M, Vallieres M, Visvikis D, Zwanenburg A. IBSI: an international community radiomics standardization initiative. J Nucl Med. 2018;59(supplement 1):287.
136. Lambin P, Rios-Velazquez E, Leijenaar R, Carvalho S, van Stiphout RGPM, Granton P, et al. Radiomics: Extracting more information from medical images using advanced feature analysis. Eur J Cancer. 2012;48(4):441–6.
137. Haralick RM, Shanmugam K, Dinstein I. Textural features for image classification. IEEE Trans Syst Man Cybern. 1973;3(6):610–21.
138. Avanzo M, Wei L, Stancanello J, Vallières M, Rao A, Morin O, et al. Machine and deep learning methods for radiomics. Med Phys. 2020;47(5):e185–202.
139. Avanzo M, Stancanello J, El Naqa I. Beyond imaging: the promise of radiomics. Phys Med. 2017;38:122–39.